ERDC/CRREL TR-23-10

Cold Regions Research
and Engineering Laboratory

US Army Corps
of Engineers®
Engineer Research and
Development Center

ERDC
ENGINEER RESEARCH & DEVELOPMENT CENTER

Extreme Cold Weather

Incorporating Advanced Snow Microphysics and Lateral Transport into the Noah-Multiparameterization (Noah-MP) Land Surface Model

Theodore W. Letcher and Julie Parno

September 2023

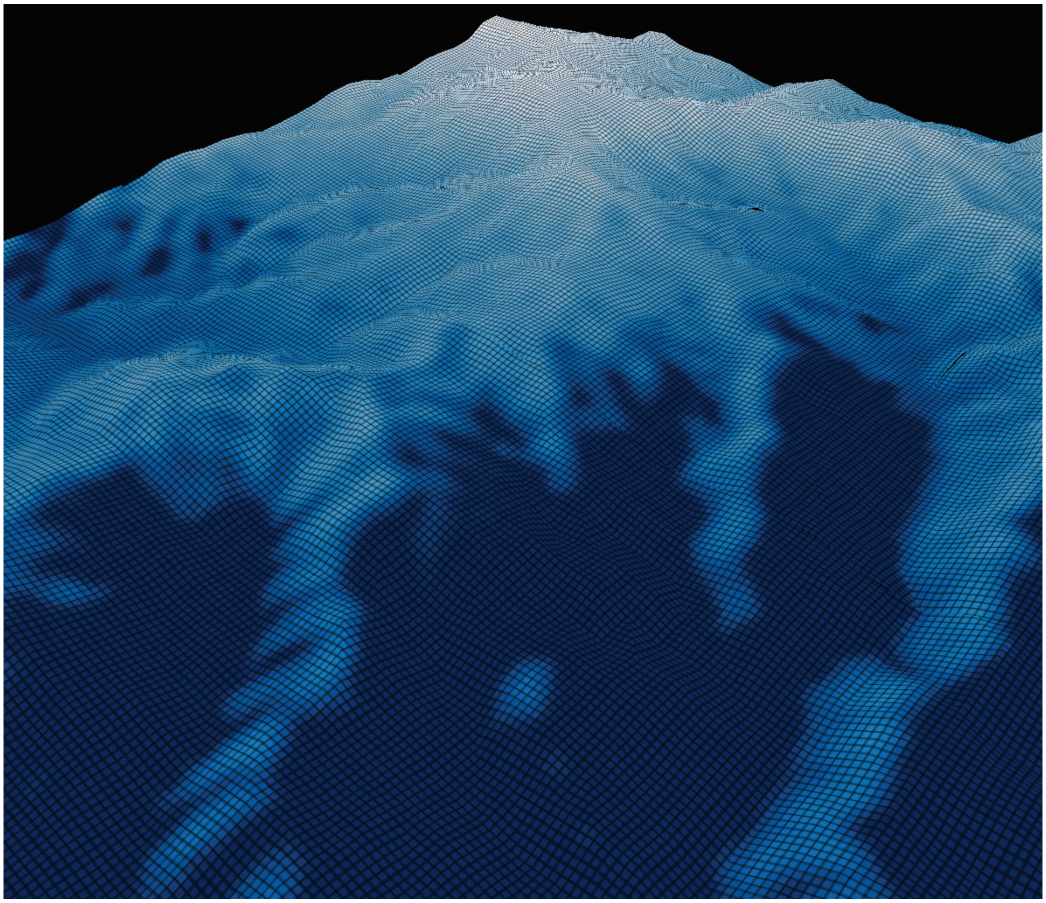

Distribution Statement A. Approved for public release: distribution is unlimited.

ERDC/CRREL TR-23-10
September 2023

Incorporating Advanced Snow Microphysics and Lateral Transport into the Noah-Multiparameterization (Noah-MP) Land Surface Model

Theodore W. Letcher and Julie Parno

US Army Engineer Research and Development Center (ERDC)
Cold Regions Research and Engineering Laboratory (CRREL)
72 Lyme Road
Hanover, NH 03755-1290

Final Technical Report (TR)

Prepared for Headquarters, US Army Corps of Engineers
Washington, DC 20314-1000

Under Program Element No. 0602144A, Project No. BN8

Abstract

The dynamic state of the land surface presents challenges and opportunities for military and civil operations in extreme cold environments. In particular, the effects of snow and frozen ground on Soldier and vehicle mobility are hard to overstate. Current authoritative weather and land models are run at global scales (i.e., dx > 10 km) and are of limited use at the Soldier scale (dx < 100 m). Here, we describe several snow physics upgrades made to the Noah-Multiparameterization (Noah-MP) community land surface model (LSM). These upgrades include a blowing snow overlay to simulate the lateral redistribution of snow by the wind and the addition of new prognostic snow microstructure variables, namely grain size and bond radius. These additions represent major upgrades to the snow component of the Noah-MP LSM because they incorporate processes and methods used in more specialized snow modeling frameworks. These upgrades are demonstrated in idealized and real-world applications. The test simulations were promising and show that the newly added snow physics replicate observed behavior with reasonable accuracy. We hope these upgrades facilitate ongoing and future research on characterizing the effects of the integrated snow and soil land surface in extreme cold environments at the tactical scale.

Contents

Figures and Tables

Figures

Tables

Preface

This study was conducted for Headquarters, US Army Corps of Engineers, under Program Element No. 0602144A, Project No. BN8. The technical monitor was Dr. Robyn Barbato.

The work was performed by the Terrestrial and Cryospheric Sciences Branch of the Research and Engineering Division, US Army Engineer Research and Development Center, Cold Regions Research and Engineering Laboratory (ERDC-CRREL). At the time of publication, Dr. John Weatherly was branch chief and acting division chief, and Dr. Robert Davis was the technical director for the Congressional Program Increase. The deputy director of ERDC-CRREL was Dr. Ivan P. Beckman, and the director was Dr. Joseph Corriveau.

The commander of ERDC was COL Christian Patterson, and the director was Dr. David W. Pittman.

1 Introduction

1.1 Background

The dynamic state of the land surface is an integral part of successful Army mission planning and execution. For example, wet soft soils hinder vehicle mobility and increase Soldier exposure in hostile terrain. In contrast, hard frozen soils can create new mobility corridors. Snow presents additional mobility challenges and Soldier hazards, such as slowed vehicle and Soldier movement, reduced visibility or whiteout conditions, and avalanche risks in the mountains (e.g., ATP 3-90.97; Milley and O'Keefe 2016). The state of the land is also a key consideration for assessing potential drought or flood risks.

One throughline connecting several of these snow hazards is blowing snow and snow transport. Snow transport is a critically important process at local and regional scales (Pomeroy and Brun 2001). In watersheds defined by high relief in complex terrain, lateral snow transport is an integral part of the hydrologic cycle because snow is blown from exposed windward slopes and deposited on the lee side of peaks and ridges. This process effects both local water resources and avalanche risk. On exposed prairies and arctic tundra, blowing snow represents an enhancement of the sublimation process and hardens the snowpack through mechanical compaction of grains at the surface (Pomeroy and Brun 2001). Accordingly, understanding and predicting the snow and soil state is an essential tool for research and operations planning.

Currently, the Air Force 557 Weather Wing (557WW) provides the authoritative dataset of global snow and soil information. This product is determined through a combination of land surface modeling and data assimilation using the Land Information System (LIS). This implementation of LIS uses the Noah community land surface model (LSM) combined with in situ and remote sensing observations to generate a forecast of the snow and soil state on a global 10 km resolution grid. The Noah LSM simulates the water mass and heat transfer through a combined land and snow column as it responds to meteorological inputs at the surface. In the near future, the underlying LSM will transition to the newer and more sophisticated Noah-Multiparameterization (Noah-MP) model, an upgraded version of the original Noah LSM (Niu et al. 2011; Yang et al. 2011).

While one of the main aspirations of the Noah-MP LSM is to provide more user control over the parameters and parameterizations used in the LSM, several significant upgrades were also made to the model physics. For example, Noah-MP improved the surface energy balance in forested regions by adding a more sophisticated forest canopy model. Additionally, substantial upgrades were made to the Noah-MP snow model. Specifically, Noah-MP replaced the original "zero-layer" snow model used in Noah with a three-layer snow model that substantially improves the insulating effects of snow (Letcher, Minder, et al. 2022). Despite these upgrades, Noah-MP is still mostly used to provide a two-way interactive lower boundary for atmospheric weather models, rather than as a tool for providing detailed information about the properties of the land and snow state. For example, the Noah-MP snow model outputs snow density (ρ_s), temperature (T_s), liquid water content (LWC), and depth (H) for each snow layer. Missing from this list are snow grain size (g_s) or snow specific area (SSA), snow grain shape, snow bond size, and snow grain orientation, which are key variables related to the mechanical and radiative properties of snow. Further, Noah-MP does not simulate blowing snow or lateral snow transport.

There are several more sophisticated snow models that simulate some or all of these processes and variables. In particular, there are a number of blowing snow transport models that are compatible with single column land models (e.g., Pomeroy et al. 1993; Liston and Sturm 1998; Déry and Yau 1999; Essery et al. 1999; Lehning and Fierz 2008; Vionnet et al. 2012; Warscher et al. 2013). However, Noah-MP has the advantage of being a widely used community model that simulates not only snow, but also the full soil column. Additionally, a growing number of studies have shown Noah-MP to perform very well at simulating the accumulation and ablation of snow (e.g., Niu et al. 2011; Cai et al. 2014; Wrzesien et al. 2015; Minder et al. 2016; You et al. 2020; Letcher, Minder, et al. 2022) and cold season soil properties (Letcher, Eylander, et al. 2022). Accordingly, adding to the suite of snowpack-state variables simulated by Noah-MP, and incorporating a snow transport model, is of substantial value as a research tool for both the US Army and the academic research community. In particular, a snow transport parameterization would make Noah-MP a much more suitable tool for simulating snow at very high (i.e., $\Delta x < 100$ m*)

---

* For a full list of the spelled-out forms of the units of measure used in this document, please refer to *US Government Publishing Office Style Manual*, 31st ed. (Washington, DC: US Government Publishing Office, 2016), 248–252, https://www.govinfo.gov/content/pkg/GPO-STYLEMANUAL-2016/pdf/GPO-STYLEMANUAL-2016.pdf.

resolution in regions where blowing and drifting snow contribute significantly to the spatial variability of snow depth.

While the addition of prognostic grain and bond size variables will not have direct effects on the bulk snow properties (e.g., snow water equivalent [SWE]), they could be leveraged to improve the treatment of snow albedo and other radiative transfer applications within the model and be relevant for other interactive and state model variables (e.g., compressive strength).

In this report, we document and demonstrate several additions made to the Noah-MP LSM that focus on adding new prognostic state variables to the snow model and on incorporating a snow transport model to a distributed version of the model.

1.2 Objective

The primary objective of this study was to document changes made to the Noah-MP LSM that increased the sophistication of the snow model. These changes primarily included adding prognostic equations that simulate microscale properties of snow relevant to radiative transfer and trafficability and a blowing snow transport model. These modifications will enable more accurate simulations of snow and soil properties at tactical scales (i.e., dx < 100 m).

1.3 Approach

To achieve the main objective, we incorporated well-validated parameterizations for blowing snow and snow microstructure into the Noah-MP LSM to enhance its capability as a field-scale modeling tool in extreme cold weather environments. This was accomplished by adding new software components to the High Resolution Land Data Assimilation System (HRLDAS) wrapper that are compatible with the Noah-MP internal core and distributed memory parallelization functionality. We demonstrated these modifications and changes using idealized and real-world simulations.

2 Data and Methods

2.1 Noah-Multiparameterization (Noah-MP)

Noah-MP is a single-column comprehensive LSM that simulates the movement of water and heat through the combined snow and soil column as it responds to meteorological input at the land surface. A complete description of Noah-MP is beyond the scope of this report; however, a brief overview of the key aspects of the model is provided here. Niu et al. (2011) provide a full description of the model.

Noah-MP is typically configured with four discrete soil layers and allows up to three discrete snow layers, though the actual number of snow layers at any given location and time is determined by the total snow depth. A surface energy balance model is used to determine the surface temperature and upper boundary conditions for a one-dimensional (1D) heat transfer model. A 1D thermal diffusion model solved using the fully implicit Crank-Nicholson technique simulates the transfer of heat vertically through the combined snow and soil column and the temperature at each snow and soil layer. A similar 1D model based on the diffusive form of Richard’s equation simulates the vertical movement of water though the soil and the soil moisture. The thermal and hydraulic properties of the soil are determined using static soil texture classification and the time-variable soil moisture and soil temperature.

Noah-MP includes a fairly sophisticated forest canopy vegetation model that includes a two-stream radiative transfer model to simulate the effects of the forest on the shortwave and longwave radiative fluxes. The canopy model also includes a canopy snow interception and unloading model based on Hedstrom and Pomeroy (1998).

Finally, Noah-MP includes numerous user-adjustable physics parameterizations and physical constants. These are described in detail as part of the National Center for Atmospheric Research (NCAR 2018) public Noah-MP release with the HRLDAS.

2.2 Noah-MP Snow Modifications

In this section, we describe the modifications made to the Noah-MP LSM to improve the characterization of snow in the model. In Noah-MP, all state variables (except for temperature) are integrated using a forward–Euler time integration scheme.

The actual transfer of heat and moisture throughout the combined snow and soil column is integrated using a fully implicit and absolutely stable Crank-Nicholson time-integration scheme.

The forward–Euler scheme approximates the time derivative at time *i* of variable *x* as follows:

$$\left(\frac{dx}{dt}\right)_i = \frac{x_i - x_{i-1}}{\Delta t}. \tag{1}$$

Therefore, x_i is simply

$$x_i = x_{i-1} + \left(\frac{dx}{dt}\right)_i \Delta t, \tag{2}$$

where Δt is the model time step. Essentially, if the time-derivative of *x* is known, the state variable *x* is straightforward to calculate. The choice to use a Euler forward method is entirely one of convenience and is appropriate here because the HRLDAS implementation of Noah-MP is noninteractive with the atmospheric forcing.

2.2.1 Grain Growth

Snow grain size and SSA are critical state variables that describe the metamorphosis of snow grains as they evolve from their dendritic state at the time of snowfall toward large, rounded grains or angular facets. In particular, the grain dry-growth rate within the snowpack is a function of vapor and temperature gradients throughout the snowpack. Grains also grow in the presence of liquid water. The addition of a multilayer snowpack in Noah-MP provides a natural model configuration for simulating snow stratigraphic properties. In this study, we simulated grain growth following the formulas presented by Jordan (1991) as part of the SNTHRM snow model, though we noted that several similar parameterizations exist for SSA in the literature (e.g., Roy et al. 2013; Vionnet et al. 2012). Jordan (1991) presented a formula that relates the dry-growth rate to the snow-layer water vapor mass flux:

$$\frac{dg_s}{dt} = \frac{g_1 |U_v|}{g_s}, \tag{3}$$

where g_s is the snow grain diameter (in meters), g_1 is an empirical grain growth parameter given as a constant 5 × 10^{-7} m^4 kg^{-1}, and $|U_v|$ is the absolute value of the snow–water vapor mass flux (in kg m^{-2} s^{-1}). It is further assumed that $|U_v|$ is proportional to the snow-layer temperature gradient:

$$|U_v| = D_{eos}\left(\frac{1000}{p}\right)\left(\frac{T}{273.15}\right)^6 C_{iT}\left|\frac{dT}{dz}\right|, \tag{4}$$

where D_{eos} is the diffusion coefficient for water vapor in snow (0.92 × 10^{-4} m^2 s^1), p is the air surface air pressure (hPa), T is the snow-layer mean temperature (in Kelvins), and C_{iT} is the variation of the saturation vapor pressure relative to ice (in N K m^{-2}). C_{iT} is given as

$$C_{iT} = \frac{c_1}{T^2}\left[\frac{L_{vi}}{R_w T} - 1\right] e^{-\left(\frac{L_{vi}}{R_w T}\right)}, \tag{5}$$

where L_{vi} is the latent heat of sublimation (L_{vi} = 2.838 × 10^6 J kg^{-1}), R_w is the water-vapor-gas constant (R_w = 461.3 J kg^{-1} K^{-1}), and c_1 is a constant given as 8.047 × 109 kg K m^{-3}. Combining the equations yields an equation for the dry-growth rate for snow grains:

$$\frac{dg_s}{dt} = \frac{g_1}{g_s} D_{eos}\left(\frac{1000}{p}\right)\left(\frac{T}{273.15}\right)^6 \frac{c_1}{T^2}\left[\frac{L_{vi}}{R_w T} - 1\right] e^{-\left(\frac{L_{vi}}{R_w T}\right)}\left|\frac{dT}{dz}\right|. \tag{6}$$

The Noah-MP model is configured using a discretization that places temperature, density, and LWC for layer *i* at the centroid of each grid. The layer height (H_i) is located at the top of layer *i*. Accordingly, the temperature gradient in the model is computed with temperature averaged to the top and bottom of layer *i*:

$$\left(\frac{dT}{dz}\right)_i = \left(\frac{\Delta T}{\Delta z}\right)_i = \frac{0.5(T_{i+1} - T_{i-1})}{H_i - H_{i-1}}. \tag{7}$$

For wet snow growth, a simpler equation that simulates the growth of large snow grains at the expense of melting small grains is used:

$$\frac{dg_s}{dt} = \begin{cases} \frac{g_2}{g_s}(\theta_l + 0.05), 0.0 < \theta_l < 0.09 \\ \frac{g_2}{g_s}(0.14), 0.09 < \theta_l \end{cases}, \tag{8}$$

where θ_l is the volumetric LWC in m^3 m^{-3} and g_2 is a constant equal to 4 × 10^{-12} m^2 s^{-1}.

The size of the bonds linking snow grains within a snowpack is an important variable that relates to snow erodibility and snow compressive strength. Here, we implemented a parameterization for bond radius (r_b) growth to support snow erodibility. This parameterization is from the SNOWPACK model (Brun et al. 1992; Brown et al. 2001; Lehning, Bartelt, Brown, Fierz, and Satyawali 2002; Lehning, Bartelt, Brown, and Fierz 2002). This parameterization breaks the dry-growth rate of snow grains into an equilibrium growth regime and a strong gradient growth regime. Under equilibrium growth, grain bonds grow according to their size and shape and are calculated as

$$\frac{dr_b}{dt} = A_0 S\left[e^{\frac{-B_1}{r_n}} - e^{\frac{B_1}{r_g}}\right] exp\left(B_2^{\left(\frac{1}{273.15}-\frac{1}{T}\right)}\right), \tag{9}$$

where A_0, B_1, and B_2 are constants equal to 1.436×10^{-7} m s^{-1}, 1.885×10^{-9} m, and 4.669×10^{3} K, respectively; S is the particle sphericity, which ranges between 0 and 1 and defines the degree of roundness of a snow particle (Brun et al. 1992); r_g is the grain radius ($g_s/2$); and r_n is the thermodynamic bond neck radius given as

$$r_n^{-1} = 2\left(\frac{1}{r_b} - \frac{1}{r_c}\right), \tag{10}$$

where r_c is the concave particle radius:

$$r_c = \frac{r_b^2}{2(r_g - r_b)}. \tag{11}$$

Under the strong temperature gradient growth regime (dT/dz > 10 K), the bond-radius growth is given as the following:

$$\frac{dr_b}{dt} = \frac{D_{eos} L e_{s,i}}{\rho_{ice} R^2 T^3}\left(\frac{dT}{dz}\right)_{\mu b}\left(\frac{r_g^2}{r_b L} - \frac{r_b}{2L}\right), \tag{12}$$

where R is the dry gas constant (R = 287 J kg^{-1} K^{-1}), and $e_{s,i}$ is the saturation vapor pressure over ice:

$$e_{s,i} = 611\, exp(0.0857T - 273.15). \tag{13}$$

L is the bond-neck radius, which is computed as

$$L = \frac{2r_g {r_b}^2}{2r_g(r_g - r_b) + r_g {r_b}^2}. \quad (14)$$

The temperature gradient of the microbonds between particles is expressed as a function of the snow-layer temperature gradient:

$$\left(\frac{dT}{dz}\right)_{\mu b} = \frac{\lambda_s}{\lambda_i}\frac{A}{A_b}\left|\frac{dT}{dz}\right|. \quad (15)$$

The thermal conductivity of ice (λ_i) is taken to be constant at 2.2 W m^{-1} K^{-1}. The thermal conductivity of snow is a function of density and can be calculated as follows:

$$\lambda_s = 2.22\left(\frac{\rho_s}{1000}\right)^{1.88}. \quad (16)$$

In the equation that follows, A_b is the cross-sectional area of the bond given as a function of grain radius:

$$A_b = \pi {r_b}^2. \quad (17)$$

In Equation (18), A is the mean cross-sectional radius of the grains, bonds, and pores combined:

$$A = \frac{(A_g + A_b + A_p)}{3}, \quad (18)$$

where A_g and A_p follow the same formulization as A_b. The pore radius is expressed this way:

$$r_p = \left(P\frac{{r_g}^3}{1-P}\right)^{\frac{1}{3}}, \quad (19)$$

where P is the porosity

$$P = 1 - \frac{\rho_s}{\rho_{ice}}. \quad (20)$$

For a more detailed description of the preceding formulas for bond dry growth under different growth regimes, refer to Brun et al. (1992), Brown et al. (2001), and Lehning, Bartelt, Brown, Fierz, and Satyawali (2002).

2.2.2 Lateral Snow Transport

The snow surface is composed of snow grains with varying sizes and shapes. This granular surface is susceptible to erosion by the wind, which can initiate blowing snow and lateral snow transport. Blowing snow is an aeolian process that is somewhat analogous to blowing sand or dust. This process is initiated as mechanical energy from the wind is transferred to the surface and directly dislodges larger snow grains from the surface. These larger grains then hop along the surface because they are typically too heavy to be entrained out of the surface layer into the atmosphere. As they hop along the surface, they dislodge additional grains. Taken together, the movement of larger grains along the snow surface is referred to as *saltation*. As saltation occurs, smaller grains are dislodged from the surface, and a portion of these smaller grains is entrained into the atmospheric boundary layer through a process referred to as *turbulent suspension*. While there is no obvious distinction between these two processes, the aeolian modeling community often considers these processes to be separate.

2.2.2.1 Erodibility

The erodibility of a snow surface is a critical variable that controls the rate of snow transport. Specifically, it dictates the amount of surface wind stress required to initiate particle mobilization and has significant influence on the saltation flux at a given location. Accordingly, the flux of blowing snow out of the saltation layer and into the boundary layer also strongly depends on the erodibility of the snow surface.

Snow surface erodibility is essentially a function of the strength and number of the intergrain bonds at the surface (Schmidt 1980; He and Ohara 2017). Another important control on erodibility is grain shape, which controls the aerodynamic forces upon a grain surface and its susceptibility to fracture or disaggregation (Schmidt 1980; Clifton et al. 2006; Comola et al. 2017). The erodibility of a snow surface is typically quantified using the threshold friction speed (u_t^*), which is the minimum friction speed (u^*) required to initiate saltation. There are several different parameterizations for u_t^*, with varying complexity, in the literature. In keeping with the multiparameterization ethos of Noah-MP, we implemented several available parameterizations:

1. The threshold friction speed (u_t^*) is given a user-specified constant value.

2. Following Li and Pomeroy (1997), u_t^* is given as a polynomial empirical function of 2 m air temperature:

   $$u_t^5 = 9.43 + 0.18T_{air} + 0.0033{T_{air}}^2, \qquad (21)$$

   where u_t^5 is the threshold wind speed at 5 m above the surface, and T_{air} is the air temperature. Then, u_t^5 can be converted to a threshold friction speed assuming a neutrally stable log wind profile:

   $$u_t^* = \kappa \frac{u_t^5}{\ln\left(\frac{5}{z_0}\right)}, \qquad (22)$$

   where κ is the Von Kármán constant (~0.4), and z_0 is the surface roughness of snow (approximately 0.002 m).
3. Following Liston et al. (2007), u_t^* is given as a function of snow density:

   $$u_t^* = \begin{cases} 0.1\, e^{0.003\rho_s}, \rho_s \le 300 \\ 0.005 e^{0.013\rho_s}, \rho_s > 300 \end{cases}, \qquad (23)$$

   where ρ_s (in kg m^{-3}) is either the bulk snow density (if there is only one snow layer) or the snow density of the top snow layer.
4. As is used in the SNOWPACK model (Lehning and Fierz 2008), u_t^* is given as a function of grain size, shape, bond size, and coordination number:

   $$u_t^* = \sqrt{\left(\frac{A_c g \rho_{ice} r_g (S+1) + B\sigma N_3 \frac{{r_b}^2}{{r_g}^2}}{\rho_{air}}\right)}, \qquad (24)$$

   where A_c and B are constants equal to 0.02 and 0.0015, respectively, σ is a reference shear strength set constant to 300 Pa, g is the gravitational constant (9.81 m s^{-2}), and ρ_{air} is the air density (kg m^{-3}). The coordination number (N_3) is given following Golubev and Sokratov (2004),

   $$N_3 = exp\left(0.705{A_{sn}}^2 + 1.57\right), \qquad (25)$$

   where A_{sn} is a function of both the snow density and the looseness parameter (k_{loose}),

   $$A_{sn} = \frac{\rho_s}{\rho_{ice}} \frac{6}{\pi} {k_{loose}}^3, \qquad (26)$$

   and k_{loose} is given as

   $$k_{loose} = S\frac{2}{2.1} + 0.45(1 - S)\left(2.91 - \frac{r_b}{r_g}\left[2.10 - \frac{r_b}{r_g}\right]\right). \qquad (27)$$

> This corresponds to the weighted values for spherical and nonspherical particles given in Golubev and Sokratov (2004).

A comparison between these four parameterizations shows large differences in the representation of surface erodibility (Figure 1). In particular, the parameterization from Liston et al. (2007) produces very erodible snow for snow densities as high as 300 kg m^{-3}. In contrast, the Li and Pomeroy (1997) parameterization never yields a value lower than the 0.3 m s^{-1} constant threshold value. The Lehning and Fierz (2008) parameterization has a weak dependence on density and is more strongly dependent on grain size. For instance, a grain diameter of 0.1 mm yields a u_t^* lower than 0.2 m s^{-1} at all densities, whereas a grain diameter of 0.4 mm yields a u_t^* near the 0.3 m s^{-1} threshold. This strong dependence of u_t^* on grain size indicates that accurate values of grain size, and in particular initial values associated with new snow, are essential for accurately characterizing the surface erodibility with this parameterization.

Figure 1. Comparison of the parameterizations for u_t^*. The *dashed black line* in each figure shows a commonly used constant 0.3 m s⁻¹ value. For the Lehning and Fierz (2008) parameterization, the sphericity is assumed to be 0.5, and the bond radius is assumed to be 10% of the grain radius.

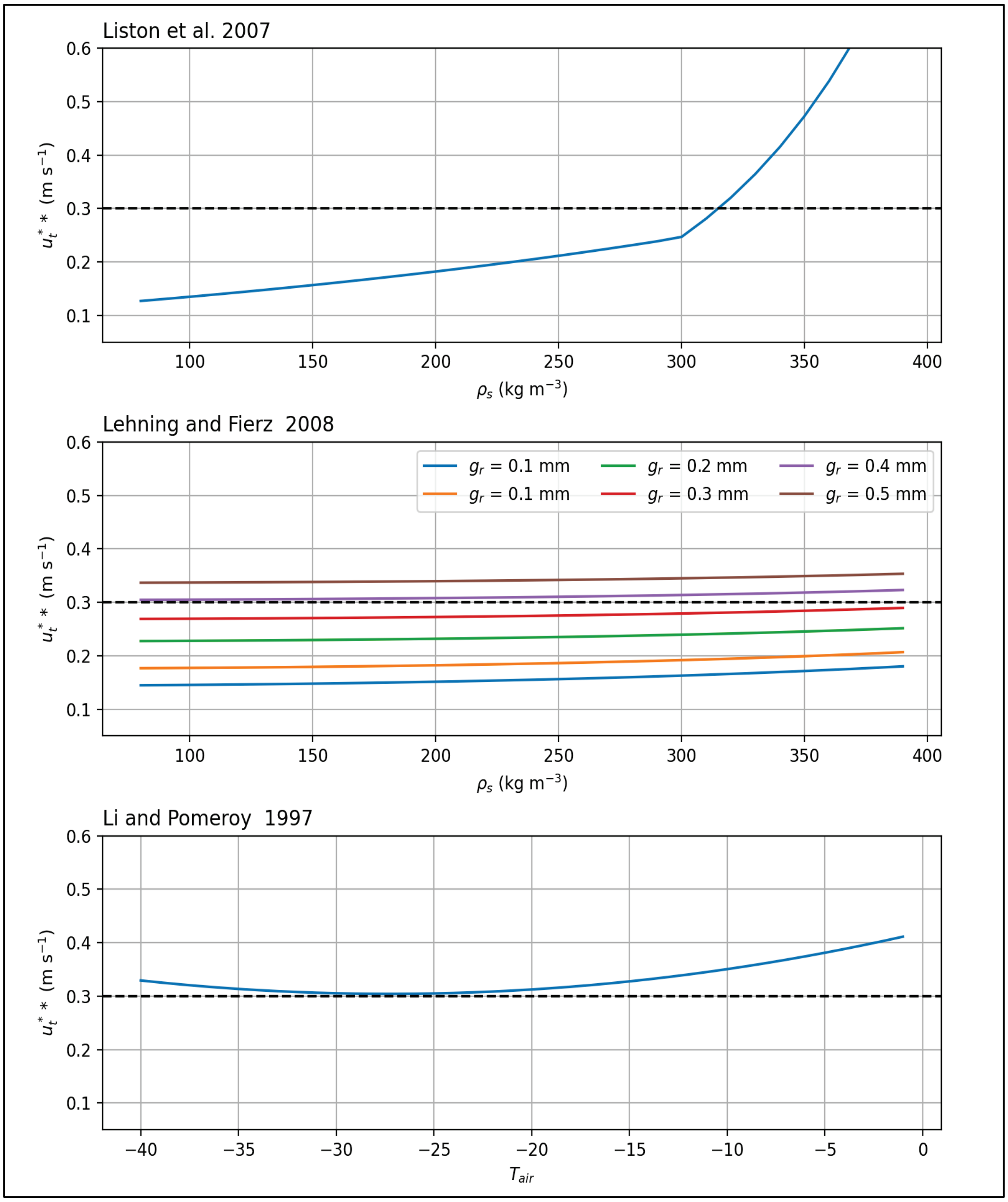

2.2.2.2 *Blowing Snow*

In this section, we detail the addition of a blowing snow and snow transport overlay into Noah-MP that can be used when Noah-MP is run in a distributed configuration through the HRLDAS. The snow transport overlay serves as an additional source or sink for snow for each grid cell because snow can be transferred from one grid cell to a neighboring grid cell.

For example, according to Liston and Sturm (1998) and Marsh et al. (2020), the local (i.e., grid-cell) change in snow mass due to blowing snow and snow transport is expressed as the horizontal convergence of the streamwise blowing snow mass fluxes:

$$\left(\frac{d\zeta}{dt}\right)_{blowing\ snow} = -\left(\frac{dQ_{s,x}}{dx} + \frac{dQ_{t,x}}{dx} + \frac{dQ_{s,y}}{dy} + \frac{dQ_{t,y}}{dy}\right), \tag{28}$$

where ζ is the snow mass in kg m^{-2} (or mm water equivalent), and Q_s and Q_t are the streamwise blowing snow mass fluxes within the saltation layer and the boundary layer in kg m^{-1} s^{-1}, respectively. This is written more formally as the convergence of fluxes:

$$\left(\frac{d\zeta}{dt}\right)_{blowing\ snow} = -\vec{\nabla} \cdot \left(\overrightarrow{Q_s} + \overrightarrow{Q_t}\right). \tag{29}$$

To suppress high-frequency noise excited by the centered-in-space, forward-in-time numerical integration, a diffusion term is added:

$$\left(\frac{d\zeta}{dt}\right)_{blowing\ snow} = -\vec{\nabla} \cdot \left(\overrightarrow{Q_s} + \overrightarrow{Q_t}\right) + D\alpha_n \nabla^n \zeta, \tag{30}$$

where D is a user-adjustable scaling factor that ranges between 0 and 1, and, following Xu (2000), α_n is a scaling constant proportional to the diffusion order (n), time step, and grid spacing:

$$\alpha_n = -1^{\frac{n}{2}+1} \frac{1}{dt} \left(\frac{dx}{2}\right)^n. \tag{31}$$

This smoothing technique is similar to techniques applied in other numerical models (e.g., the Weather and Research Forecast model) and targets spurious oscillations excited by nonlinear interactions within the model. Therefore, α_n is computed such that the shortest (i.e., $2\Delta x$) waves will be 100% eliminated over a single time step (Xue 2000). The D scaling constant allows users to more gradually reduce noise. Critically, the diffusion scheme here is applied directly to SWE and is, therefore, active at every grid cell, regardless of whether or not snow is actively blowing. This can lead to artificially smooth snow solutions in the distributed SWE fields over long periods without new snowfall. To mitigate this, we recommend using generally small values of D (e.g., $D < 0.05$). Diffusion will be discussed in more detail in Section 2.2.2.6.

Because Equation (28) represents a change in snow mass (i.e., SWE), a corresponding change in depth (H) is required. For simplicity, the snow height is changed assuming no local change in snow density:

$$\left(\frac{dH}{dt}\right)_{blowing\ snow} = \frac{1}{\rho_s}\left(\frac{d\zeta}{dt}\right)_{blowing\ snow}. \tag{32}$$

Instead, snow density changes due to blowing snow are applied where the surface wind stress is sufficient to initiate snow transport. This is discussed in Section 2.2.2.5.

For grid cells where the change in snow mass due to blowing snow is less than zero, the snow depth is adjusted to accommodate the loss of SWE without changing the density. An additional change to snow density due to surface wind stress applied at all grid cells is discussed in Section 2.2.2.5.

2.2.2.3 Saltation

There are numerous parameterizations for the Q_s in the literature (Pomeroy and Gray 1990; Pomeroy et al. 1993; Lehning and Fierz 2008; Vionnet et al. 2012). These parameterizations are based on a combination of first principal physics and empirical formulas and are often analogous to parameterizations used in other aeolian models. In all cases, Q_s is a function of the difference between the surface wind stress expressed as the friction speed (u^*) and the threshold friction speed (u_t^*) in m s^{-1}. The friction speed can be related to the near surface windspeed at height z above ground level (AGL) using a log wind profile:

$$u^* = \psi \frac{\kappa U_z}{\ln\left(\frac{z}{z_0}\right)}, \tag{33}$$

where U_z is the scalar wind speed at z, and ψ is a stability correction that scales log profile according to the near-surface atmospheric stratification. The stability correction function can be quite complicated and has known issues over snow (Barlage et al. 2010; Niu et al. 2011). While this correction is critically important for computing the turbulent heat and momentum fluxes at the snow surface under calm, stable conditions, for simplicity, we assumed that $\psi = 1$, which is indicative of neutral stability.

We hypothesized that this is generally a good assumption for situations where the wind is strong enough to mobilize snow because the strong winds act to mix the near-surface layer, leading to neutral stability.

The surface roughness length over a snow-covered surface (z_0) is complicated by the fact that in many instances, nonerodible elements, such as rocks or vegetation, stick up out of the snow. Without explicitly accounting for nonerodible elements in the blowing snow saltation scheme, the increased surface roughness caused by protruding elements would, counter-intuitively, increase the saltation flux because the friction speed would be increased according to Equation (33). Accordingly, if the vegetation roughness is incorporated in the surface roughness for blowing snow, the saltation parameterization should also include a drag partition that divides the applied wind stress into erodible and nonerodible elements.

Here, we provide three parameterizations for the simulated stream-wise saltation flux (Q_s) in the Noah-MP.

1. The parameterization described in Pomeroy and Gray (1990) as adapted by Liston and Sturm (1998)
2. The parameterization presented in Pomeroy et al. (1993), which includes a drag partition to account for nonerodible surface elements
3. The parameterization presented by Marsh et al. (2020), which is similar to that discussed in list entry 2 but with a modified drag partition

These three options for saltation can be accessed through the HRLDAS namelist variable "blowing_snow_salt_opt."

In each instance, the surface friction speed follows Equation (33). The surface roughness (z_0) is taken to be either Z0SNO, specified in the MPTABLE.TBL file that is included with the HRLDAS framework, or it is determined as a function of air temperature following Keenan et al. (2022):

$$z_{0,snow} = \begin{cases} 0.002, T_{air} \leq -20°\text{C} \\ 10e^{-\left(\frac{0.4}{\sqrt{C_{ND}}}\right)}, T_{air} > -20°\text{C} \end{cases}, \tag{34}$$

where C_{ND} is the neutral drag coefficient at 10 m and is a function of air temperature equal to

$$C_{ND} = 2.3 \times 10^{-3} + 9 \times 10^{-5}(T_{air} - 273.15) + 1.5 \times 10^{-6}(T_{air} - 273.15)^2. \quad (35)$$

Once the surface roughness and friction speed have been calculated, an initial saltation flux (Q_s) is calculated in one of the three ways that follow:

1. In Pomeroy and Gray (1990), it is calculated this way:

$$Q_s = \frac{0.68}{u^*}\frac{\rho_{air}}{g}u_t^*\left(u^{*2} - u_t^{*2}\right). \quad (36)$$

For option 1 (Pomeroy and Gray 1990), we followed the implementation described in Liston and Sturm (1998), which accounts for the coupling between z_0 and u^* that occurs under an actively eroding surface. This is accomplished using a Newton-Ralphson iterative process that solves for z_0:

$$0 = \frac{0.12}{2g}\left(\frac{\kappa U_z}{ln\frac{z}{z_0}}\right)^2 - z_0. \quad (37)$$

A maximum value of z_0 = 0.15 is set for the snow surface to eliminate the possibility of numerical instabilities in Equation (37). Because there is no representation of nonerodible surface elements in Equation (35), it is assumed that the surface is 100% snow covered and free of obstructions to ensure that u^* is not overly strong.

2. The second option for saltation is from Pomeroy et al. (1993) and is nearly identical to the first, except that it includes nonerodible elements:

$$Q_s = \frac{0.68}{u^*}\frac{\rho_{air}}{g}u_t^*\left(u^{*2} - {u_n^*}^2 - u_t^{*2}\right), \quad (38)$$

   where ${u_n^*}^2$ is introduced as the friction speed applied to the nonerodible elements (i.e., the amount of surface stress applied to fixed-surface features such as rocks or vegetation).

The formulation described in Pomeroy et al. (1993) was primarily focused on the effect of vegetation protruding through the snow pack, and accordingly, the parameters that go into calculating u_n^* are associated with plant elements. Here, u_n^* is determined as

$$u_n^* = \left(1 - \frac{1}{C_r}\right), \quad (39)$$

where C_r is a roughness constant, which is defined as

$$C_r = 1.638 + 17.04 N_{st} H_{st} D_{st} - 0.117. \tag{40}$$

N_{st}, H_{st}, and D_{st} are the element (or stalk) density, height above the snow, and diameter, respectively. It is assumed that $N_{st} = 25\ \text{m}^{-1}$ and $D_{st} = 3$ mm. H_{st} is the difference between a user-prescribed vegetation height and the snow surface:

$$H_{st} = \max\left(Z_{snow} - Z_{veg}, 0\right). \tag{41}$$

Z_{veg} is the assumed vegetation height, usually on the order of 10–40 cm, that can be prescribed by the user through the namelist value "blowing_snow_vg_hgt." Because Q_s has a drag partition, the surface roughness is the combined roughness of the snow and the nonerodible elements:

$$z_0 = \frac{0.12 u^{*2}}{2g} + \frac{N_{st} H_{st} D_{st}}{2}. \tag{42}$$

By including the nonerodible elements, z_0 is increased, leading to an increased u^*. In addition, if $H_{st} = 0$, Equation (42) reduces to the equation described in Liston and Sturm (1998). Similar to the first parameterization, the Newton-Ralphson iterative process is used to solve for z_0 and u^* simultaneously.

3. The final parameterization for Q_s is as described in Marsh et al. (2020):

$$Q_s = \frac{0.68 u_t u^* \rho_{air}}{g}\left(1 - \frac{{u_n^*}^2}{u^{*2}} - \frac{u_t^{*2}}{u^{*2}}\right). \tag{43}$$

This parameterization is nearly identical to the previous one, except the treatment of nonerodible elements is slightly different. Here, nonerodible elements are characterized as

$$\frac{{u_n^*}^2}{u^{*2}} = \frac{m\beta_d N_{st} H_{st} D_{st}}{(1 + m\beta_d N_{st} H_{st} D_{st})}, \tag{44}$$

where m and β_d are constants assumed to be 0.16 and 202, respectively (Marsh et al. 2020).

Then z_0 and u^* are determined as in Equations (33), (37), and (42).

Once Q_s is computed, it is then scaled independently for the x and y directions to attain the maximum streamwise saltation fluxes (as expressed in

Equation 45). This requires that, for each direction, Q_s is scaled proportionally by the associated vector wind components (Liston and Sturm 1998):

$$Q_{s,x,max} = \frac{u}{U} Q_s, \tag{45}$$

$$Q_{s,y,max} = \frac{v}{U} Q_s,$$

where u and v are the x and y components of the wind, respectively, and U is the 10 m windspeed. These are then scaled to account for the effect of fetch on the mobilization of snow grains along the surface. The fetch is applied using a hyperbolic tangent scaling, following Marsh et al. (2020):

$$f_{fetch} = \frac{\tanh\left(\frac{4L_{fetch}}{f_{eq}} - 2\right)}{2} + 0.5, \tag{46}$$

where f_{eq} is an equilibrium fetch value, set to 350 m, and L_{fetch} is the fetch distance. The fetch distance L_{fetch} is computed independently in x and y and is computed as the distance from a sign change in the respective wind component following the component direction. For example, following from west to east, the fetch increases by the grid-spacing (Δx) for each grid with $u > 0$. Once a value of $u < 0$ is reached along the path, L_{fetch} is reset to zero. L_{fetch} remains zero following the path until a value of $u > 0$ is reached, and the process starts over. This computation is performed for the west-to-east, east-to-west, south-to-north, and north-to-south directions, resulting in an L_{fetch} vector ($\vec{L}_{fetch} = (L_{fetch,x}, L_{fetch,y})$). The final saltation flux at each grid cell is then

$$Q_{s,x} = f_{fetch}(L_{fetch,x}) \frac{u}{U} Q_s, \tag{47}$$

$$Q_{s,y} = f_{fetch}(L_{fetch,y}) \frac{v}{U} Q_s.$$

Finally, if the land cover classification of the grid cell is one of the forested categories, the total grid cell average saltation flux is the combination of saltation flux computed for the forested and nonforested areas of the grid cell weighted by the canopy fraction:

$$Q_{s,x} = f_{forest} Q_{s,x,forest} + \left(1 - f_{forest}\right) Q_{s,x,bare}, \tag{48}$$

$$Q_{s,y} = f_{forest} Q_{s,y,forest} + (1 - f_{forest}) Q_{s,y,bare},$$

where f_{forest} is the canopy fraction. $Q_{s,forest}$ is computed exactly as described previously, except U is first scaled to the zero-displacement height within the canopy (Liston and Elder 2006a):

$$U_{forest} = U e^{-0.36 LAI}, \tag{49}$$

where LAI is the leaf-area index. The only thing that this modification affects within the Q_s parameterizations is the surface friction speed (u^*).

2.2.2.4 Turbulent Suspension

Once the saltation fluxes have been calculated, turbulent suspension fluxes are computed based on the saltation flux, following Pomeroy and Male (1992), Liston and Sturm (1998), and Vionnet et al. (2014). First, the height of the saltation layer (H_{salt}) and mean particle speed (u_p) are determined from the friction and threshold friction speeds:

$$H_{salt} = \frac{u^{*2}}{2g}, \tag{50}$$

$$u_p = 2.8 u_t^*.$$

Then, a reference-level blowing snow particle concentration (in kg m^{-3}) is computed following Vionnet et al. (2014):

$$q_{ref} = \frac{Q_s}{u_p} \frac{0.45g}{u^{*2}} e^{-\frac{0.45 H_{salt} g}{u^{*2}}}. \tag{51}$$

Finally, the total turbulent suspension flux (Q_{susp}) along the x and y directions is calculated by integrating the blowing snow concentration multiplied by the appropriate wind component throughout the lower boundary layer:

$$Q_{susp,x} = u_{ref} q_{ref} H_{salt} + \int_{z=H_{salt}}^{\infty} u_z q_z dz, \tag{52}$$

where u_{ref} is wind speed at the saltation layer top (H_{salt}), u_z is wind speed at height z determined from a neutrally stable log profile, and q_z is the blowing snow concentration at z, given by Pomeroy and Male (1992):

$$q_z = q_{ref} exp(-1.55[0.05628u^*]^{-0.544} - z^{-0.544}). \tag{53}$$

In the implementation of this model, the integral is approximated by summing between H_{salt} and 2.5 m AGL:

$$Q_{susp,x} = u_{ref} q_{ref} H_{salt} + \sum_{z=H_{salt}}^{2.5} u_z q_z \Delta z. \tag{54}$$

A sublimation term is also calculated following Schmidt (1982), as implemented in several blowing snow models. The rate of loss due to sublimation is described in Pomeroy et al. (1993) and Liston and Sturm (1998), which is heavily based on work by Schmidt (1991). The following equations describing blowing snow sublimation are reproduced from Liston and Sturm (1998) and Pomeroy et al. (1993). This parameterization essentially computes a particle-mass normalized loss rate (s^{-1}) and applies it to the blowing snow concentration at height z,

$$Q_{sub,z} = \varphi_{sub,z} q_z dz, \tag{55}$$

where Q_{sub} is the sublimation rate in units of kg m^{-2} s^{-1} (mm s^{-1} water equivalent) and φ_{sub} is the sublimation loss rate,

$$\varphi_{sub} = \frac{1}{\overline{m_p}} \frac{d\overline{m_p}}{dt}, \tag{56}$$

where $\overline{m_p}$ is the mean particle mass. The mean particle mass is assumed to be a function of height:

$$\overline{m_p}(z) = \frac{4}{3}\pi \rho_{ice} \overline{r_p}^3 \left(1 + \frac{3}{\alpha_p} + \frac{2}{\alpha_p{}^2}\right), \tag{57}$$

where $\overline{r_p}$ is the mean particle radius and α_p is a shape parameter, both assumed to be a function of height,

$$\overline{r_p}(\mathrm{z}) = 4.6 \times 10^{-5} z^{-0.258}, \tag{58}$$

$$\alpha_p = 4.08 + 12.6z. \tag{59}$$

The time rate of change of the mean particle mass is given by

$$\frac{d\overline{m_p}}{dt} = \frac{2\pi \overline{r_p} \sigma - \frac{S_p}{\lambda_{atmo} T_{air} Nu}\left[\frac{L_{vi} M_w}{R_u T_{air}} - 1\right]}{\frac{L_{vi}}{\lambda_{atmo} T_{air} Nu}\left[\frac{L_{vi} M_w}{R_u T_{air}} - 1\right] + \frac{1}{D_v \rho_v Nu}}. \tag{60}$$

In Equation (60), λ_{atmo} is the thermal conductivity of the atmosphere (0.024 J m^{-1} s^{-1} K^{-1}), M_w is the molar weight of water (18 kg mol^{-1}), and R_u is the universal gas constant (8,313 J $kmole^{-1}$ K^{-1}). D_v, ρ_v, and S_p are the diffusivity of water vapor, the saturation vapor density, and the solar radiation absorbed by the particle, respectively. Definitions for each of these follow. Nu is the Nusselt number given as a function of the Reynolds number (R_e):

$$Nu = 1.79 + 0.606\sqrt{R_e}. \tag{61}$$

The Reynolds number is the ratio between the inertial forces acting on the particle to the fluid viscosity of the air and is a function of z:

$$R_e(z) = \frac{2\,\overline{r_p}V_v}{\nu}, \tag{62}$$

where ν is the kinematic viscosity of air (1.3×10^{-5} m^2 s^{-1}). V_v is the ventilation velocity and accounts for the particle fall speed ($\overline{w_p}$) and turbulence production near the surface

$$V_v = w_p + 2.21\,x_r, \tag{63}$$

where x_r is the fluctuating velocity component given as a function of height (Pomeroy 1988):

$$x_r(z) = 0.005{U_z}^{1.36}. \tag{64}$$

Particle fall speed ($\overline{w_p}$) is a function of the particle radius size, which also varies with height:

$$\overline{w_p}(z) = 1.1\ \times 10^7\overline{r_p}^{1.8}. \tag{65}$$

D_v is the diffusivity of water vapor in the atmosphere, given as

$$D_v = 2.06\ \times\ 10^{-5}\left(\frac{T_{air}}{273}\right)^{1.75}, \tag{66}$$

and σ is the under saturation with respect to ice. This is downscaled within the near surface layer, following Déry and Taylor (1996),

$$\sigma(z) = \sigma_r\big(\ \Gamma + 0.027\ln(z)\big), \tag{67}$$

where σ_r is the under saturation at the reference level (assumed to be 2 m AGL):

$$\sigma_r = RH_{2\mathrm{m}} - 1. \tag{68}$$

The RH lapse-rate, Γ, is

$$\Gamma = 1 - 0.027\ln(z_{2\mathrm{m}}). \tag{69}$$

S_p is the solar radiation absorbed by the particle,

$$S_p = \pi\bar{r}_p^{\,2}\left(1 - \alpha_p\right)(1 + \alpha_s)\mathrm{SW}^{\downarrow}, \tag{70}$$

where α_p is the particle albedo, assumed to be 0.6, α_s is the surface albedo provided by the model, and $\mathrm{SW}^{\downarrow}$ is the downwelling solar radiation (in W m^{-2}). The saturation vapor density (ρ_v) is given as

$$\rho_v = 0.622\frac{e_s}{R_d T_{air}}, \tag{71}$$

where R_d is the dry gas constant (287 J K^{-1} kg^{-1}) and e_s is the saturation vapor pressure over ice:

$$e_s = 610.78exp\left(\frac{21.875(T_{air} - 273.16)}{T_{air} - 7.66}\right). \tag{72}$$

2.2.2.5 *Drift Density*

As snow is blown and drifted, the snow density at the surface increases through mechanical destruction of snow particles and compaction (Clifton et al. 2006). This process is represented here in a relatively simplistic way, not altogether dissimilar to the method employed in Vionnet et al. (2012) in that the snowpack density increases relative to a characteristic time-scale. Here, the rate of compaction follows a simplified scaling such that the new snow density at time *t + 1* is

$$\rho_{s,t+1} = \rho_{s,t+}(u^* - u_n^* - u_t^*)^2\left(\rho_{drift} - \rho_s\right)\frac{\Delta t}{600}, \tag{73}$$

where ρ_{drift} is an assumed density of fully wind-compacted snow. This density adjustment is applied to the topmost layer of the snowpack. The 600 in the denominator is a characteristic timescale (in seconds) that is tuned such that the density approaches its drift density after 12–48 hours of continuous blowing snow. If $\rho_s > \rho_{drift}$ or $(u^* - u_n^* - u_t^*) < 0$, then the density is not modified by snow transport.

2.2.2.6 Numerical Integration

The blowing snow transport scheme is implemented in Noah-MP using the forward–Euler time discretization on the Arakawa C-grid (i.e., centered in space, forward in time). That is, the streamwise saltation and suspension fluxes (Q_s, Q_y) are computed on the grid-cell edges such that spatial derivatives of Q_s and Q_y are computed for the grid-cell centers where the model state variables are located. This is enforced by staggering the saltation fluxes through spatial averaging:

$$Q_{s,x,i+\frac{1}{2}} = \frac{1}{2}\left(Q_{s,x,i+1} + Q_{s,x,i}\right), \tag{74}$$

where i is the grid-cell index and the ½ notation indicates the grid-cell edge. Then, the spatial derivative of $Q_{s,x,i}$, is simplified to

$$\frac{dQ_{s,x,i}}{dx} = \frac{0.5\left(Q_{s,x,i+1} - Q_{s,x,i-1}\right)}{\Delta x}. \tag{75}$$

The diffusion term in Equation (29) is computed using higher even-order finite differencing. Here we use the sixth diffusion because it seems best able to smooth high frequency oscillations without significantly degrading the simulation.

This diffusion is only really required for schemes where u_t^* is a function of the snowpack characteristics (e.g., snow density) because these characteristics are directly impacted by changes in SWE. The finite difference form of sixth-order diffusion is presented in Equation (74). For brevity, only the x-component is shown:

$$\nabla_x^6 \zeta_{i,j} = \frac{\zeta_{i+3,j} - 6\,\zeta_{i+2,j} + 15\zeta_{i+1,j} - 20\zeta_{i,j} - 15\zeta_{i-1,j} - 6\zeta_{i-2,j} + \zeta_{i-3,j}}{\Delta x^6}. \tag{76}$$

One critical aspect of this snow transport model is that it has inherent issues because snow is a finite quantity. That is, no intrinsic physics within this model prohibit it from removing more snow than there is available at any given grid cell. For simplicity, we addressed this contingency by simply setting the SWE equal to zero at any grid cell where the snow transport model removed more snow than was available. This ensured that the snow transport model did not result in negative SWE values being passed to the internal Noah-MP physics. We acknowledge that this is a crude adjustment that is not mass-conserving. However, we anticipate the effect of this simplification to be generally small because there are some additional restrictions in place that do not allow for saltation to occur at snow-free grid cells.

2.2.3 Adaptation of Snow Transport to Fortran Message-Passing Interface (MPI)

The single-column nature of the Noah-MP LSM makes it a good candidate for parallelization on a high-performance computing system such as the DoD High-Performance Computing Modernization Program (HPCMP). Specifically, because each grid cell is independent in the standard configuration, the computations can easily be farmed out to an arbitrary number of computer nodes that work independently from one another in parallel, greatly reducing the wall time (i.e., the amount of time it takes for a simulation to complete) for a given simulation. This is illustrated schematically in Figure 2.

Figure 2. Schematic illustrating the parallel processing architecture of the Noah-Multiparameterization (Noah-MP) driver with the High Resolution Land Data Assimilation System (HRLDAS). The *different color* grid cells illustrate some arbitrary variable (e.g., terrain).

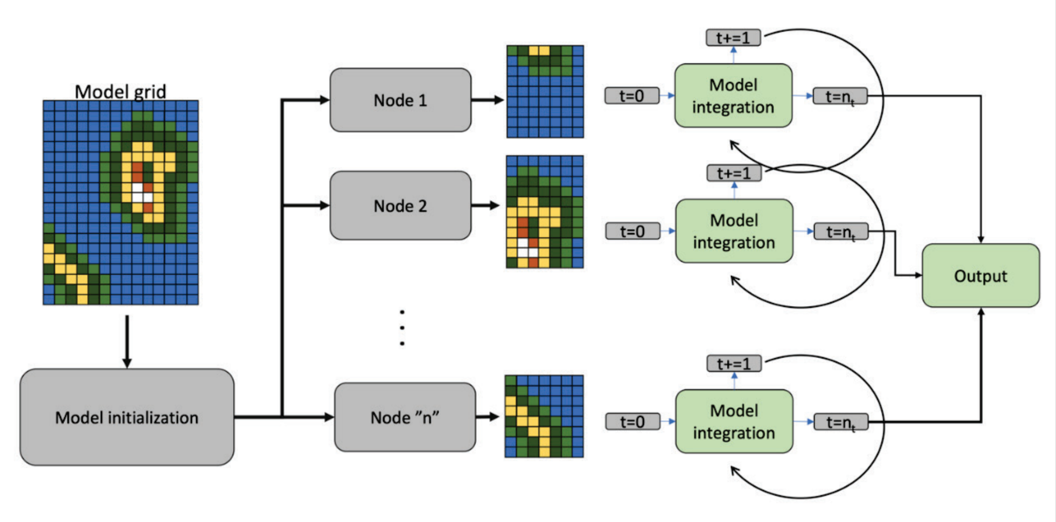

The current Noah-MP driver framework associated with the HRLDAS driver is already configured to run in parallel through use of the Fortran message-passing interface (MPI). However, the introduction of lateral snow transport creates complications for parallel computing because it requires communication between adjacent grid cells. Specifically, grid cells on the node edges require special treatment to perform the communication across nodes.

Here we use the MPI functions *send*, *receive*, and *barrier* to communicate across adjacent nodes. First, the MPI barrier function pauses model integration at a specific point in the code and waits until all of the computer nodes reach the specified point. Then the send function pulls data from the right-most grid cell from a given node, and the receive function stores that data in a specified array. Figure 3 illustrates how this process is used to compute spatial derivatives along the node boundaries.

Figure 3. Illustration of internodal communication through the message-passing interface (MPI). The *red font* indicates a grid cell associated with node 2.

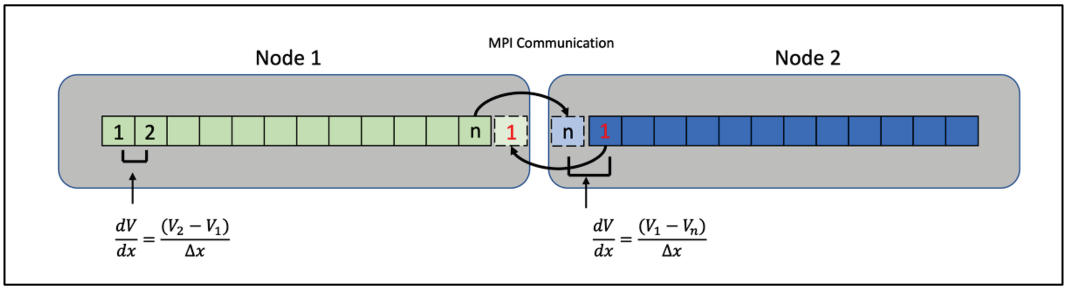

For this work, all simulations were performed using the DoD HPCMP Cray-XE super-computing systems with an Intel compiler and multiprocessing capability. Critically, these code adaptations have not been tested using a single processor environment.

2.3 Model Configuration

2.3.1 Forcing Data

Accurately representing the meteorological forcing that drives the model is key to an accurate Noah-MP model run. Small-scale wind patterns are particularly important for simulating lateral snow transport. However, there is clearly a scale mismatch between the highest resolution gridded reanalysis products and the mesoscale models (which operate on the 1 km < dx <10 km scale) and the tactical scales (dx < 100 m) desired for this work. To close this gap, a downscaling procedure is required. For all simulations in this report, the SnowModel downscaling technique MicroMet (Liston and Elder 2006b) is used to distribute coarser scale meteorological data to a finer grid. In this procedure, an optimal interpolation subroutine generates a gridded dataset by spatially weighting meteorological input from specified geographic locations across the model domain while accounting for any missing data. Once the point data have been distributed across the domain, the resulting meteorological fields are adjusted according to climatological relationships between weather and elevation. While more sophisticated downscaling techniques are becoming available, MicroMet is computationally relatively lightweight, robust, and easy to apply. For details on the downscaling process used in MicroMet, refer to Liston and Elder (2006b). However, no forest canopy effects on the meteorology are employed during MicroMet because these effects are simulated in Noah-MP.

2.3.2 Idealized Simulations

To assess the newly integrated snow transport scheme within Noah-MP, we completed idealized simulations with a single, north-south-elongated, bell-shaped hill that was 400 m tall and placed in the center of an 8×8 km^2 domain (Figure 4). The domain grid spacing was 30 m in both x and y. The model was integrated for one month beginning on 1 January for a domain with a mean latitude of 64.6°N, such that solar radiation effects were minimal. The temperature was initialized at −7.1°C and slowly increased to −6.1°C at the end of the model integration. The relative humidity was fixed at 75% throughout the simulation, and the wind was northerly and varied semirandomly between 2 and 5 m s^{-1}. Finally, for the first 40 hours of the simulation, a precipitation rate of 1.1 mm hr^{-1} was prescribed. After 40 hours, no new precipitation fell. These meteorological data were downscaled and distributed to the grid using MicroMet. This generated the spatial variability in the wind field that was necessary to excite the snow transport parameterization.

Figure 4. Terrain of idealized simulation domain. The *red arrow* indicates the mean wind direction.

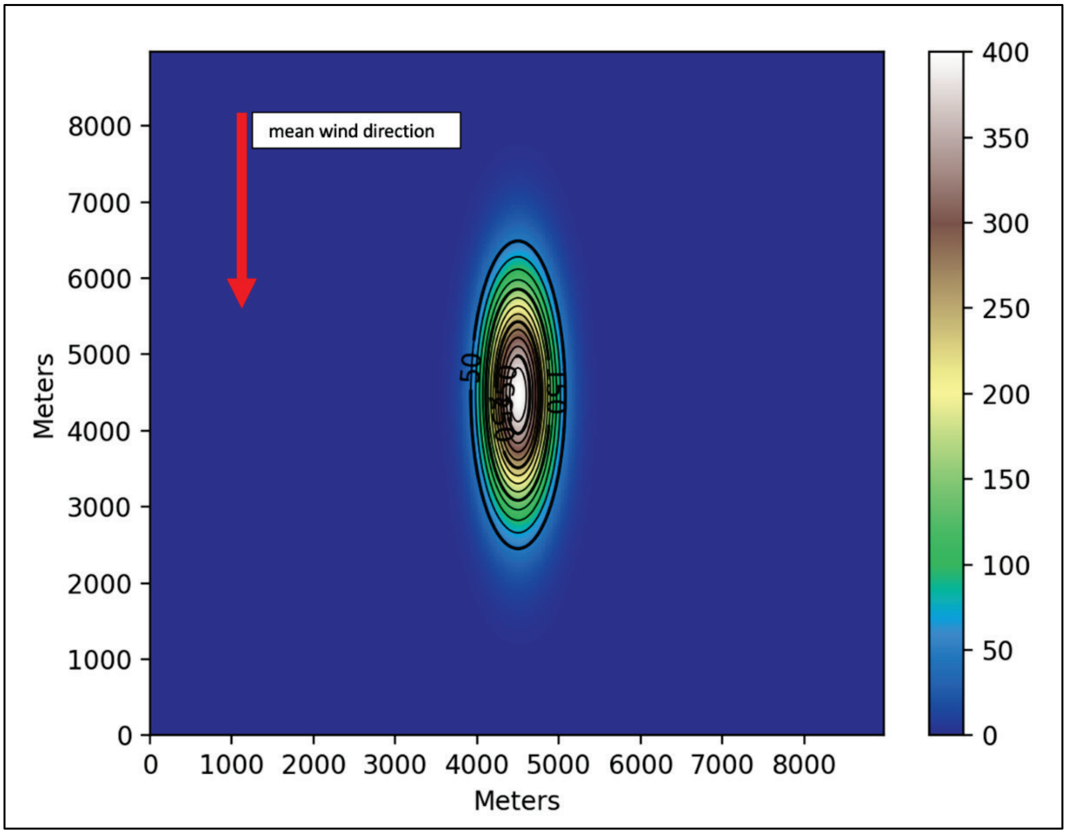

2.3.3 Dry Creek Experimental Watershed (DCEW) Simulations

To evaluate and demonstrate Noah-MP in a real-world environment, we performed two sets of simulations using distributed meteorological forcing generated from historical data collected within the Dry Creek Experimental Watershed (DCEW), which is north of Boise, Idaho (Figure 5). This watershed is a well-instrumented basin characterized by complex topography and a variety of land-cover types. Snow and weather monitoring stations are advantageously positioned at a range of elevations and within several vegetation cover types. These data are collected and maintained by the Boise State University Department of Geosciences (Boise State University, n.d.).

Figure 5. (*a*) Elevation of Dry Creek Experimental Watershed (DCEW) with locations of each weather station. (*b*) Land cover classification. The outline of the watershed is indicated by the *thick black line*. The outlined *blue rectangle* shows the subdomain used in the 10 m high-resolution simulations.

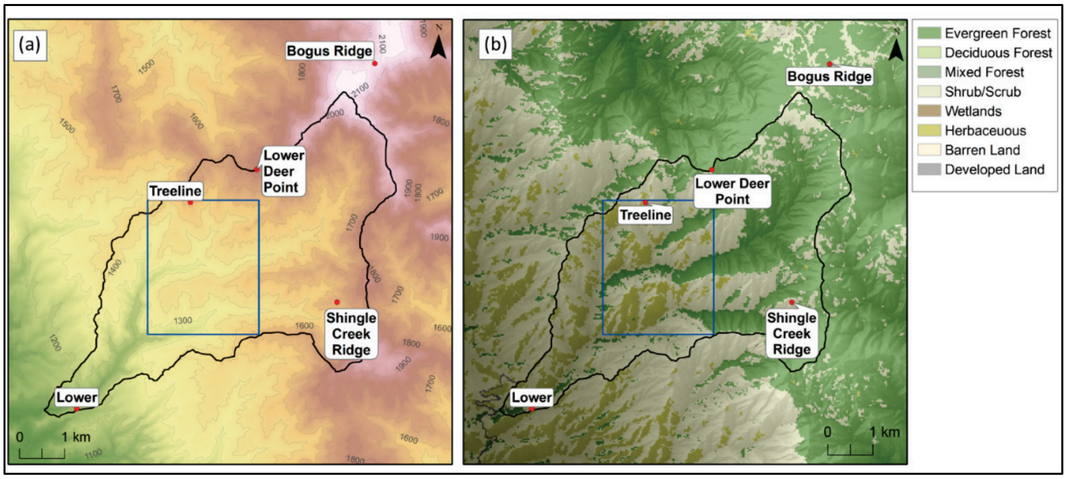

One set of simulations was focused on a large-scale, approximately 10 km × 10 km, domain with 30 m grid spacing and was performed to provide data for general model validation. The second set of simulations was performed over a smaller, approximately 2.5 km × 3 km, subdomain and was used specifically to evaluate the impacts of u_t^* on snow depth in a real-world environment. While each set of simulations had its own unique configuration, here we describe the model configuration components common to both sets of simulations.

In all of the DCEW simulations, the blowing snow saltation option from Marsh et al. (2020) with a drag partition was used. The model was run with a 300 second time step and a 0°C temperature threshold for rain and snow partitioning. Snow albedo was simulated using the Biosphere-Atmosphere Transfer Scheme (BATS) nondimensional snow age decay parameterization (Dickinson et al. 1993). All user-adjustable constants were left to their default values in the associated MPTABLE.tbl file. The sixth order diffusion operator was scaled by 0.01 in an effort to eliminate spurious oscillations without significantly affecting realistic high-frequency SWE differences caused by sharp gradients in terrain and vegetation.

The forcing for the DCEW simulations was generated by combining the observed weather station data collected within the DCEW with gridded data from the National Land Data Assimilation System (NLDAS; Mitchell et al. 2004) using SnowModel's MicroMet, as described in Section 2.3.1. Here, we chose to incorporate data from the NLDAS to provide a continuous and reliable dataset that had no missing data values. Further, to better represent the longwave radiative forcing, we used the longwave forcing and 2 m temperature from NLDAS to generate an effective atmospheric emissivity. This emissivity was then applied to the downscaled 2 m temperature from MicroMet to downscale the atmospheric longwave radiation. Finally, in addition to the slope and aspect adjustments to solar insolation calculated as part of MicroMet, we incorporated a terrain binary shadow mask that adjusted the direct solar radiation component:

$$Q_{direct} = \begin{cases} Q_{direct}, \chi = 0 \\ 0, \chi = 1 \end{cases}, \tag{77}$$

where Q_{direct} is the direct solar radiation and χ is the binary shadow mask that is equal to 1 if the grid cell is in a shadow and is equal to 0 if it is not. χ is determined by projecting the solar vector from a grid cell and checking for intersections with elevated grid cells along the vector. Additional model configurations unique to each simulation set are in Section 3.

3 Results

3.1 Idealized Comparison

We first explored the impact of snow transport within Noah-MP by using an idealized simulation focused on wind redistribution around the terrain shown in Figure 4. For this evaluation, we compared snapshots of simulated snow depth, SWE, and snow density after 23 days of elapsed time. A control simulation, in which no blowing snow transport was active, was performed. Figure 6 shows the control SWE, perturbation wind components, and convergence field.

Figure 6. (*Top left*) Simulated control snow water equivalent (SWE). (*Top right*) Perturbation *u* component of the wind. (*Bottom left*) Perturbation *v* component of the wind. (*Bottom right*) Wind convergence field. Wind is blowing from north to south, and *v* is positive, pointing toward the north.

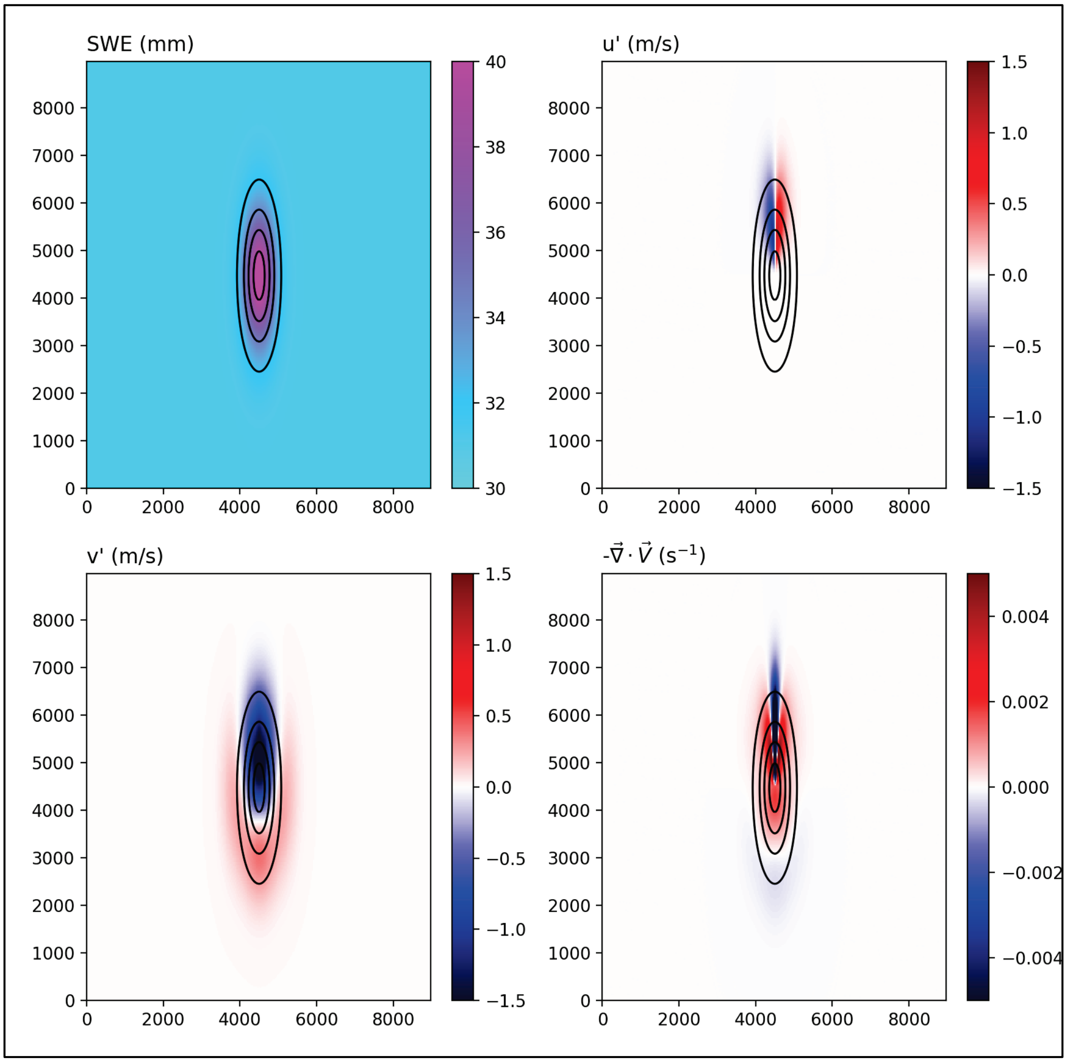

In the control simulation, the snow had a local maximum near the crest of the hill. The perturbation winds showed increased flow on the upslope side of the hill and decreased flow on the lee side. The zonal winds had downslope flow on the upwind side and no perturbation downwind of the hill crest. This led to a strong, narrow zone of divergence on the upwind slope, with convergence near and downwind of the hill crest.

To examine the blowing snow transport scheme, the SWE difference between the control simulation and each of the four u_t^* parameterizations, in addition to a fifth u_t^* that takes the average between the Li and Pomeroy (1997) and Liston et al. (2007) parameterizations, is shown in Figure 7 and outlined in Table 1.

Table 1. Parameterizations for threshold friction speed used in idealized comparison.

Option	Function	Reference
1	Constant (0.2 m s^{-1})	N/A
2	$u_t^5 = 9.43 + 0.18T_{air} + 0.0033{T_{air}}^2$	Li and Pomeroy (1997)
3	$u_t^* = \begin{cases} 0.1\, e^{0.003\rho_s}, \rho_s \leq 300 \\ 0.005e^{0.013\rho_s}, \rho_s > 300 \end{cases}$	Liston et al. (2007)
4	Average of options 2 and 3	N/A
5	$u_t^* = \sqrt{\left(\frac{A_c g \rho_{ice} r_g (S+1) + B\sigma N_3 \frac{{r_b}^2}{{r_g}^2}}{\rho_{air}}\right)}$	Lehning and Fierz (2008)

In each simulation, the snow transport function acted to move snow from the upwind side of the hill and deposit it on the downwind side. The solution using a constant $u_t^* = 0.2$ m s^{-1} had a smooth solution for all three saltation schemes, with generally small differences between them. The wind speeds imposed in this event were never enough to trigger snow transport for the Li and Pomeroy (1997) simulation. When u_t^* was determined as a function of density following Liston et al. (2007), the changes were larger and more widespread. In particular, u_t^* was low enough that snow transport was activated at every grid cell throughout the domain at least some of the time. This resulted in a uniform decrease in SWE due to sublimation across the domain where there were no convergent winds. This effect was greatest when the saltation parameterization from Pomeroy and Gray (1990) was used (PG, scheme 1; Section 2.2.2.3). When u_t^* was determined by averaging options 2 and 3 (option 4; Table 1), the snow drifting was generally limited to the elevated terrain. Similarly, the spatial extent was limited for option 5. This is because these parameterizations produced more moderate values of u_t^* (Figure 1).

Figure 7. Difference between modeled and control SWE. (*Left to right*) Namelist options controlling u_t^* 1–5 (Table 1). (*Top to bottom*) Namelist options controlling saltation schemes 1–3 (PG1990 is Pomeroy and Gray [1990], M2020 is Marsh et al. [2020], and P1993 is Pomeroy et al. [1993]). Hill topography is contoured in *black*.

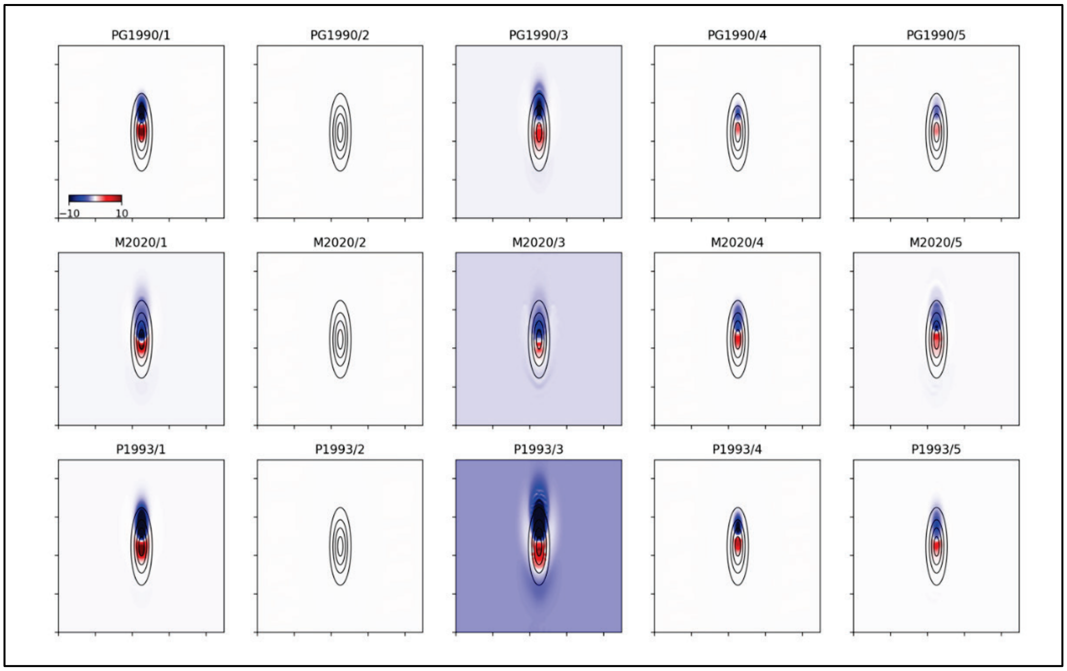

To further investigate differences between the different schemes, north-south transects of SWE, snow depth, and snow density were plotted through the middle of the hill (Figure 8). On average, the snow transport increased the SWE by a maximum of 3 mm in the lee after 30 days of integration. For all three saltation parameterizations, the constant u_t^* = 0.2 m s^{-1} resulted in the largest leeward increases in SWE, though the location of the crest was different in each parameterization. The Liston et al. (2007) u_t^* parameterization also resulted in generally large leeward SWE increases, though these were smaller than the constant u_t^*, despite the fact that Liston et al.'s u_t^* was generally less than 0.2 m s^{-1}. The smaller SWE increases were likely due to a combination of increased sublimation and a broader area where saltation was occurring.

Figure 8. (*Top to bottom*) SWE, snow depth, and snow density. *Solid blue fill* shows (from *left to right*) the south-to-north transect from the control simulation. *Each line* represents the transect from a blowing snow scheme. The *thick solid line* shows the mean over all schemes. The area *filled gray* shows the terrain (scale not shown).

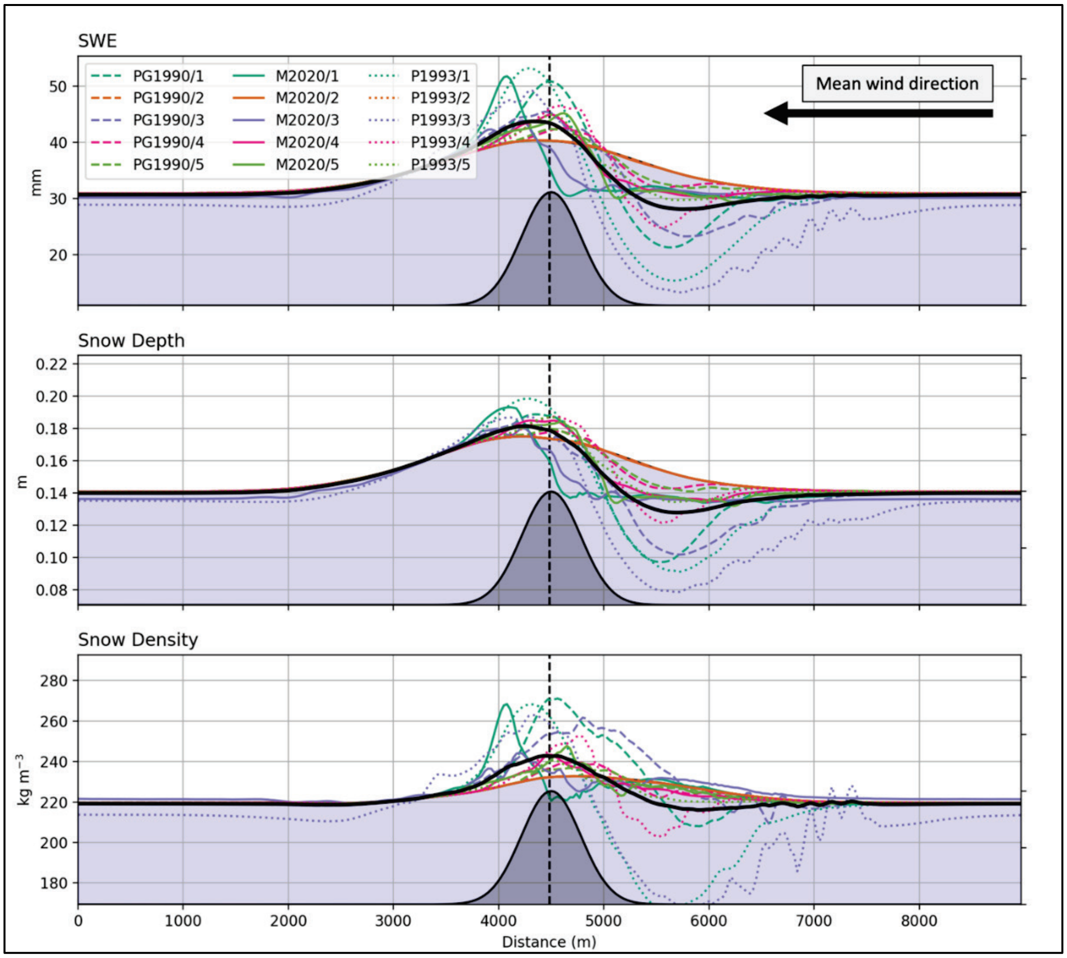

The area of removed snow was generally broader than the area of deposited snow, leading to a steeper gradient in snow depth near the hillcrest. The snow depth difference in the deposition zone was less pronounced than the SWE difference. This was largely due to a greater increase in density here that was attributable to a strong overburden densification process. While, in most cases, snow density increased everywhere when blowing snow was activated, it actually decreased in the erosion zone for the simulations that used the Pomeroy et al. (1993) saltation scheme. This scheme also produced the largest differences in SWE, both in the erosion and deposition zones. We suspect that the significantly reduced SWE in the erosion zone reduced the overburden densification so much that it counteracted the increased density caused by the snow transport. The density was the noisiest field because it was affected not only by wind, but also by changes in the amount of SWE and the snow depth.

To examine the snow microstructure, we examined a time series of domain mean snow depth, snow density, snow grain diameter, and snow bond diameter (Figure 9). The rapid decline in snow depth as the density increased was evident in the top two panels of Figure 9. Grain diameter gradually increased throughout the simulation, approaching 1.2 mm by the end of the month.

Figure 9. Time series of domain mean snow depth, density, grain size, and bond size.

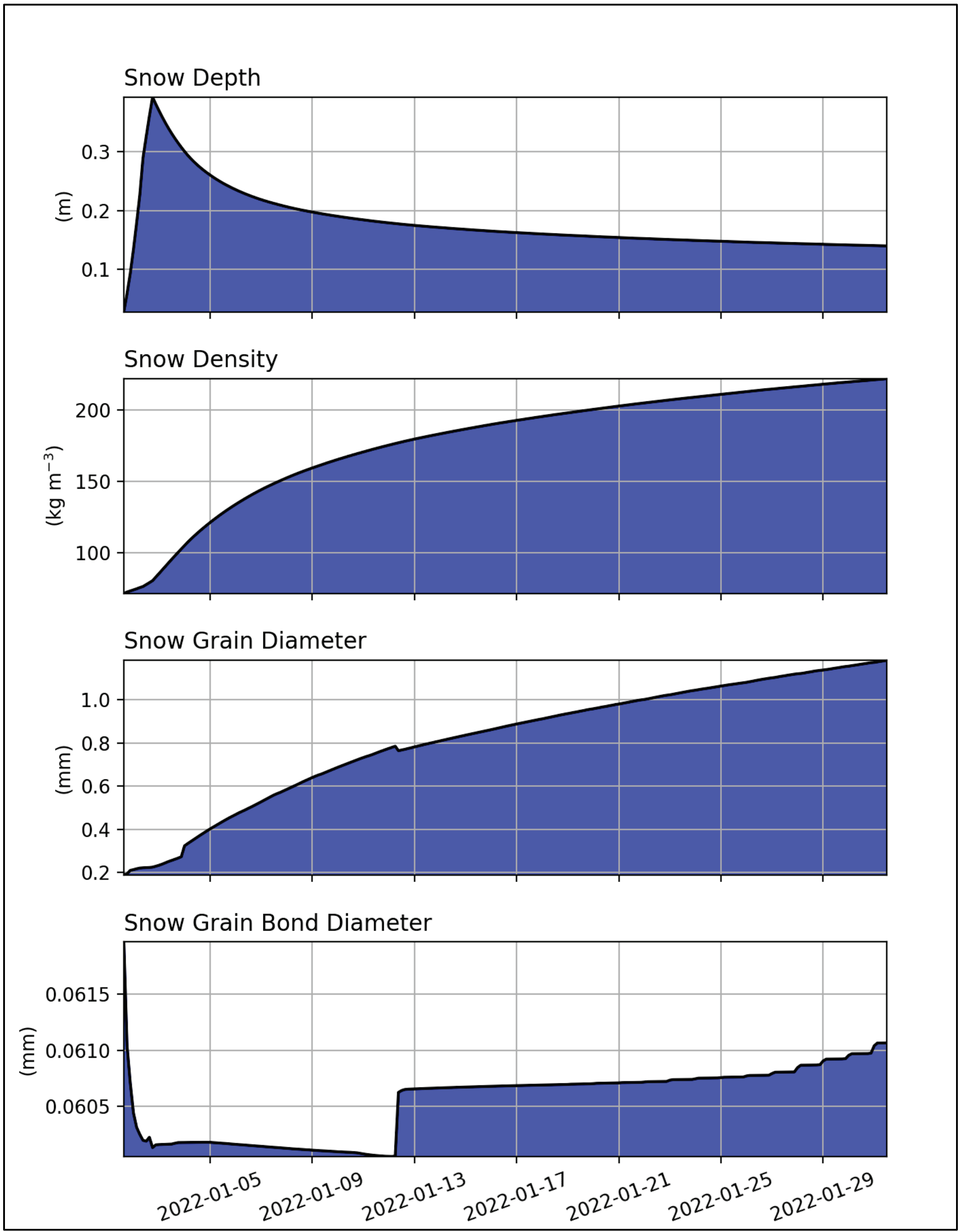

The snow bond diameter was a little less consistent, and its layer mean growth rate appeared most correlated with the number of snow layers and minor fluctuations in the solar radiation (not shown).

3.2 DCEW: Large Domain

Here we present the simulations performed over the full DCEW domain with model grid spacing equal to 30 m. The model output is evaluated against available in situ and remote-sensing data.

In addition to the configuration described in Section 2.3.3, MicroMet was used to generate hourly forcing spanning a four-year period between 1 October 2016 and 30 September 2020. To spin up the land model, the first year (October 2016–October 2017) was run five times consecutively, representing a five-year spin up period. While this was a relatively short spin up period, we felt it was acceptable for this study because we are not focused on changes in the water table or aquifer storage.

In this model configuration, u_t^* option 4 (from Table 1) was used; this option takes the average of the Li and Pomeroy (1997) and Liston et al. (2007) parameterizations.

We primarily evaluated the model-simulated snow properties to assess the model for realism. Accordingly, an initial qualitative assessment of the simulated monthly mean snow depth, density, grain diameter, threshold friction speed, soil temperature, and soil moisture for the spring melt season (Figures 10 and 11) was performed.

Figure 10. (*Left to right*) Simulated monthly mean snow depth, bulk density, and grain diameter averaged over all years for (*top to bottom*) March, April, and May. The color scales shown in the *top row* are used for each row.

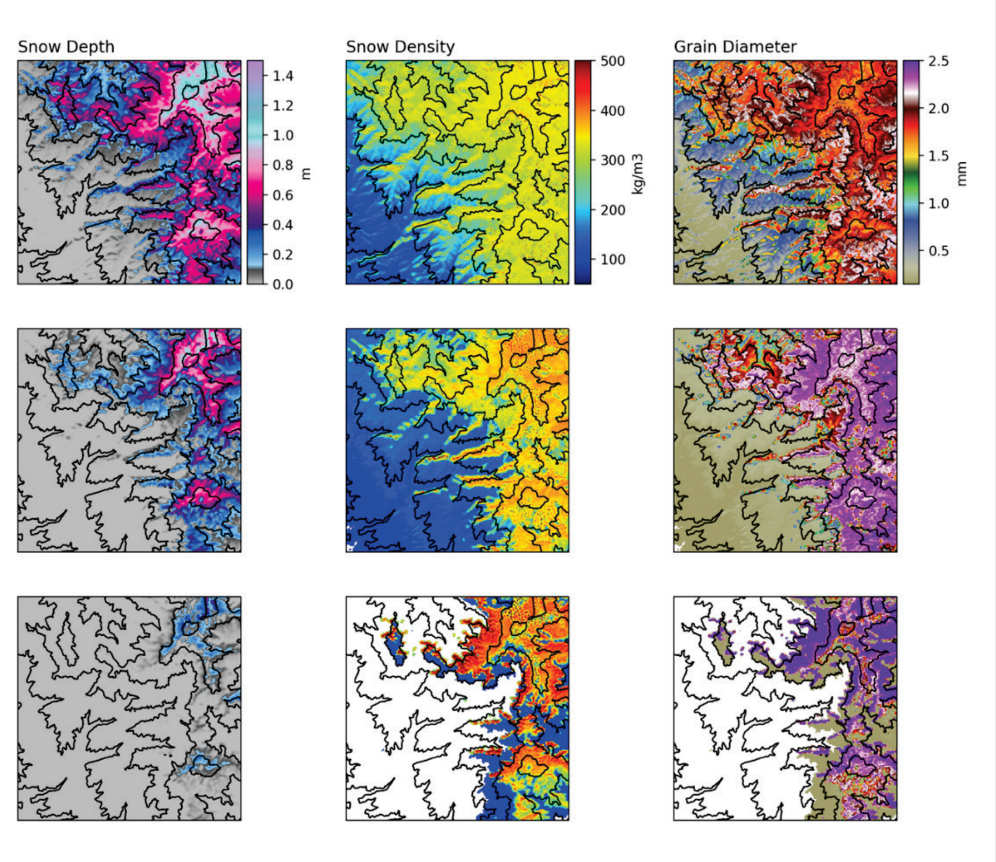

The mean snow depth was seen retreating from the more exposed low elevation regions of the domain toward the higher, tree-covered areas (Figure 10, left column). The snow depths were generally less than 1 m on average in March, except near Bogus Ridge. The average bulk density and snow grain size were seen to increase throughout the spring, consistent with the observed behavior of snow during the thaw season. The effect of the terrain aspect and the forest canopy were also evidenced in the greater snow depths and densities on forested north-facing aspects near the tree line compared to the exposed southern aspects. These patterns were consistent with the findings from Kormos et al. (2014) and Anderson et al. (2014), who both showed a substantially longer duration of snow cover on northern aspects in this region.

The threshold friction speed followed the increase in density and air temperature with elevation and season, indicating that the high elevations were most susceptible to snow transport during the colder winter, rather than during the spring when the snow was wet and dense and the air temperature was relatively warm (Figure 11). Similarly, the soil temperature warmed following the elevation and the southern aspects. In particular, the role of snow as an insulating material was evident when comparing the snow depth and soil temperature for April, showing a nearly 10°C difference between the snow-free southern aspects and the snow-covered northern aspects. Soil moisture generally followed the active snow melt, first in the middle elevations and then in the higher elevations later in the spring when the middle and lower elevations were drying out.

Figure 11. (*Left to right*) Simulated monthly mean threshold friction speed, soil temperature, and soil moisture averaged over all years for (*top to bottom*) March, April, and May. The color scales shown in the *top row* are used for each row.

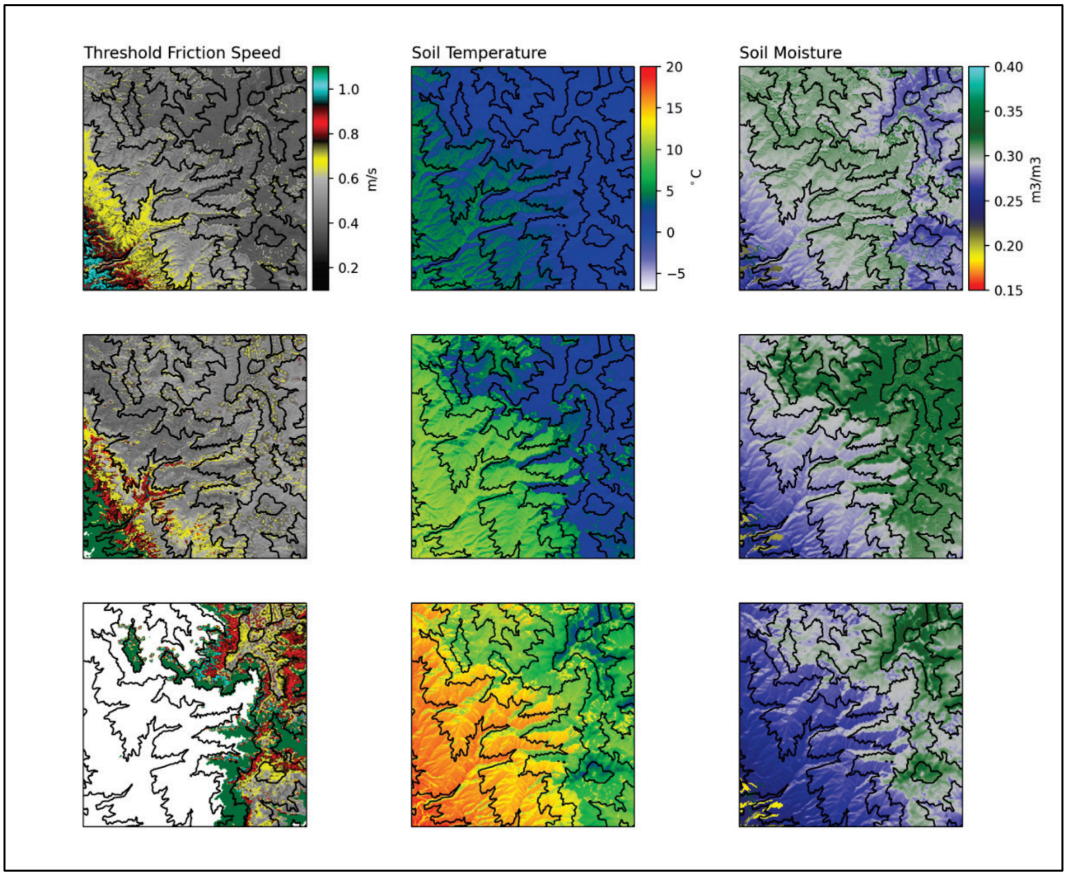

To further evaluate the snow, we first compared the simulated snow depth to measured snow depth at the five in situ snow monitoring stations throughout the domain. Figure 12 shows the simulated and observed four-year mean annual cycle in snow depth for each station. At three of the five stations, the model showed remarkable accuracy at simulating the seasonal cycle of snow depth. In particular, the model accurately simulated the peak snow depth and the melt out date.

Figure 12. Annual mean simulated and observed snow depth (in centimeters) for each station within the DCEW (locations indicated in Figure 5). The observed is *blue shaded*, and the simulated is the *thick red line*.

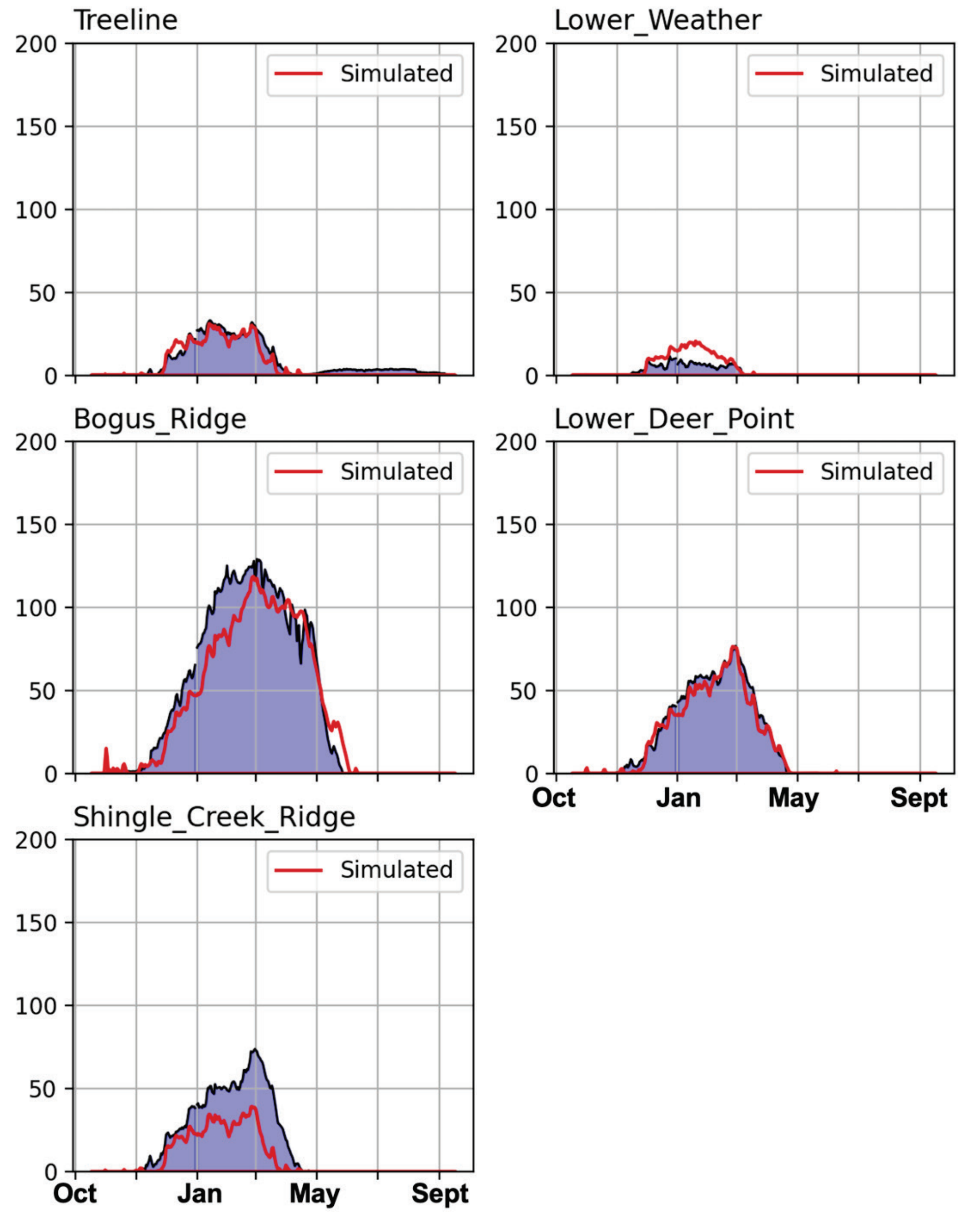

The model showed modest inaccuracy at the Shingle Creek Ridge and Lower Weather stations, where it underpredicted and overpredicted snow depth at each station, respectively. We suspect that the model was less accurate here because it is situated near the crest of a topographic ridge near the tree line, where the simulated snow is subject to higher uncertainty due to sharp gradients in forcing.

Finally, we compared the simulated snow cover fraction to a selection of available Fractional Snow-Covered Area (fSCA) maps derived from Landsat imagery. The Landsat Collection 2 fSCA is a useful tool for model validation. This dataset is freely available from the US Geological Survey and provides the percentage of pixel covered by snow for Landsat 4–8 data. It is generated from Landsat Collection 2 US Analysis Ready Data Surface Reflectance and Top of Atmosphere Reflectance data (Selkowitz et al. 2017). The data are processed to 30 m spatial resolution, which is conveniently the same as our model. For this study, we selected Landsat fSCA images that were cloud free and within the domain. The year 2019 had the most cloud-free images throughout the melt season, allowing for a look at model performance over the course of the snow season (Figure 13). Each image was reprojected to North American Datum of 1983 (NAD83)/Idaho Transverse Mercator (EPSG: 8826) and clipped to the domain. Figure 13 shows the difference between the model and Landsat fSCA for easier visualization of the discrepancies.

The Noah-MP model overestimated the snow cover extent compared to Landsat for each of the available observation dates. This was especially true for the 29 January comparison, which showed broad overestimates in snow cover fraction at most grid cells. During the spring thaw season, the Noah-MP fSCA overestimate seemed to be consistent for the transition elevations on the northern aspects, suggesting that the effects of slopes or the forest canopy on incident shortwave radiation may be overestimated by the model. This difference was most stark for the 11 March comparison, which showed extensive overestimates in fSCA on northerly aspects and corresponding underestimates in fSCA on southerly aspects. It was unclear from this set of simulations if this apparent bias was due to model physics internal to Noah-MP or if it was due to simplifications made to estimate the diffuse fraction of incident radiation in MicroMet.

Figure 13. Comparison between Noah-MP simulated and measured Landsat Fractional Snow- Covered Area (fSCA) for three different dates within the winter and spring of 2019: (*top to bottom*) 29 January, 11 March, and 19 April.

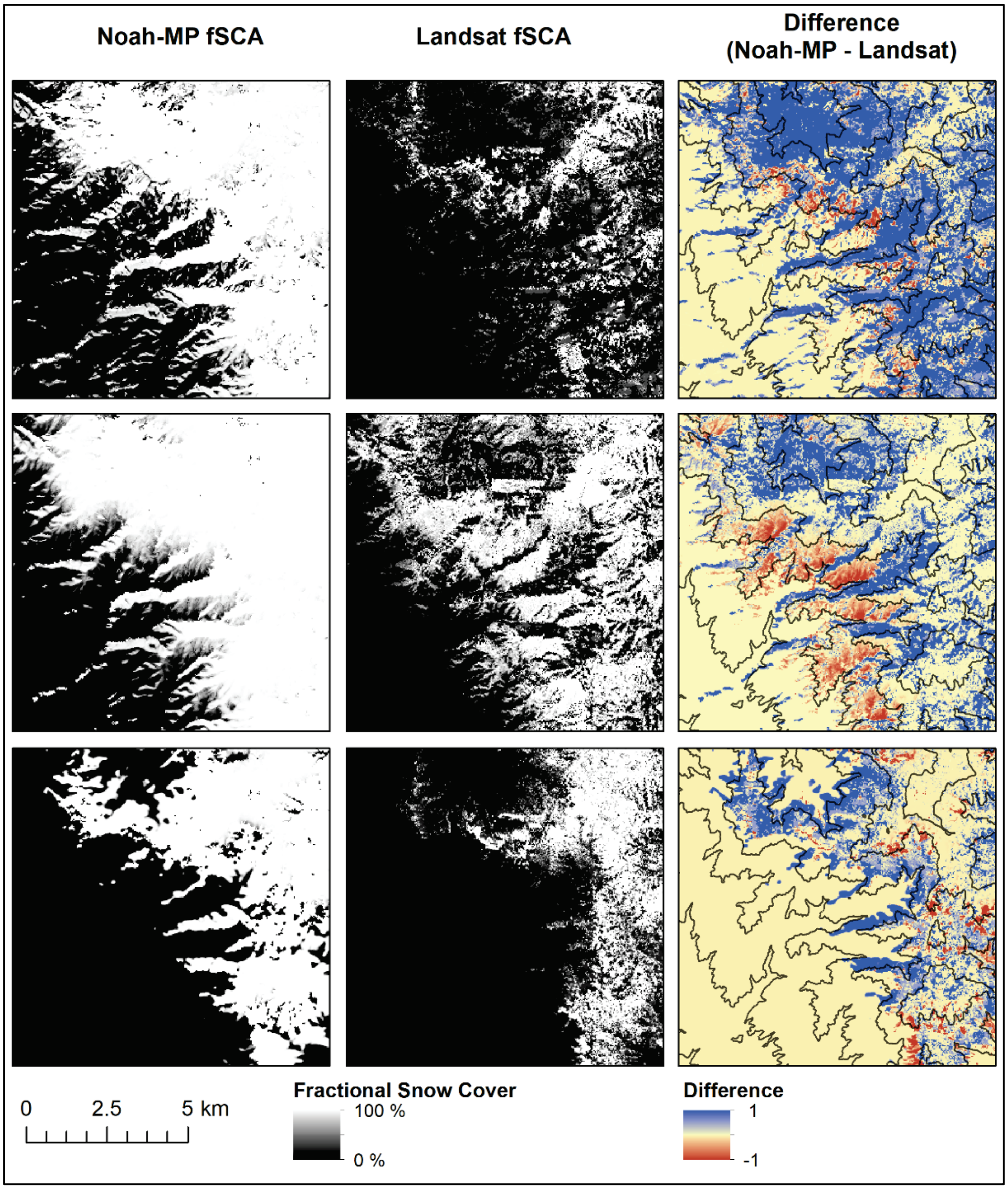

3.3 Real World Case: DCEW Subdomain

As a final demonstration of the modeling framework, we performed 6 one-year-long simulations spanning 1 October 2019 through 1 October 2020 at 10 m resolution for a subdomain of the DCEW as a way to investigate the effects of the different u_t^* options on the simulated snow depth. The six simulations included one control simulation with blowing snow turned off and five experimental simulations corresponding to each of the 5 u_t^*

parameterizations (Table 1). Figures 14 and 15 show simulated monthly mean u_t^* and snow depth differences for February 2020, respectively.

The u_t^* option 2 (threshold friction velocity [UST]2), which follows the air-temperature-based formula from Li and Pomeroy (1997), showed very limited variability across this domain and was generally near 0.4 at all grid cells. In contrast, the Liston et al. (2007) parameterization (option 3; UST3) showed high variability and favored very low u_t^* values on northern aspects. The highest u_t^* values tended to follow ridge crests where blowing snow was likely increasing the snow density. The u_t^* option 4 (UST4), which averages options 2 and 3, showed the same spatial variability as UST3, but with a weaker magnitude. Option 5 (UST5), which was the most complicated of the available options, was most similar to 4, though with substantially higher u_t^* on northern aspects. In this option, u_t^* tended to fall between 0.25 and 0.5 m s^{-1}, with a few locations exceeding 0.7 m s^{-1} along ridge crests, where drifting increased snow density, or at the valley floor, where snow was likely starting to melt.

The February mean changes in snow depth reflect both the effects of u_t^* and the wind patterns. Specifically, the general patterns of the snow depth changes were consistent for all simulations, but their magnitudes were strongly tied to the u_t^* option used. Unsurprisingly, the greatest changes in snow depth were seen with UST3, which had the lowest u_t^* values. The changes associated with UST2 were almost negligible due to the restrictively high u_t^* values. In all cases, however, the greatest snow depth changes were focused along the ridgelines and on local-scale ridge features along northern aspects, which were the most wind-exposed under mean westerly flow regimes. The overall magnitude of these changes was relatively small, compared to the mean snow depth, but was not negligible. For example, snow depth differences were generally on the order of magnitude of 10 cm for a snow depth averaging between 20 and 60 cm, representing an up to 50% change in snow depth for all u_t^* options except UST2. These effects generally lessened throughout the spring thaw season and had only a minimal effect on the domain average soil moisture and temperature (not shown).

Figure 14. Simulated February mean $\boldsymbol{u}_t^*$ for $\boldsymbol{u}_t^*$ options 2 (*top left*), 3 (*top right*), 4 (*bottom left*), and 5 (*bottom right*). Option 1 is not shown because it is held constant at 0.25. Elevation contours are shown in *black* with an 80 m interval.

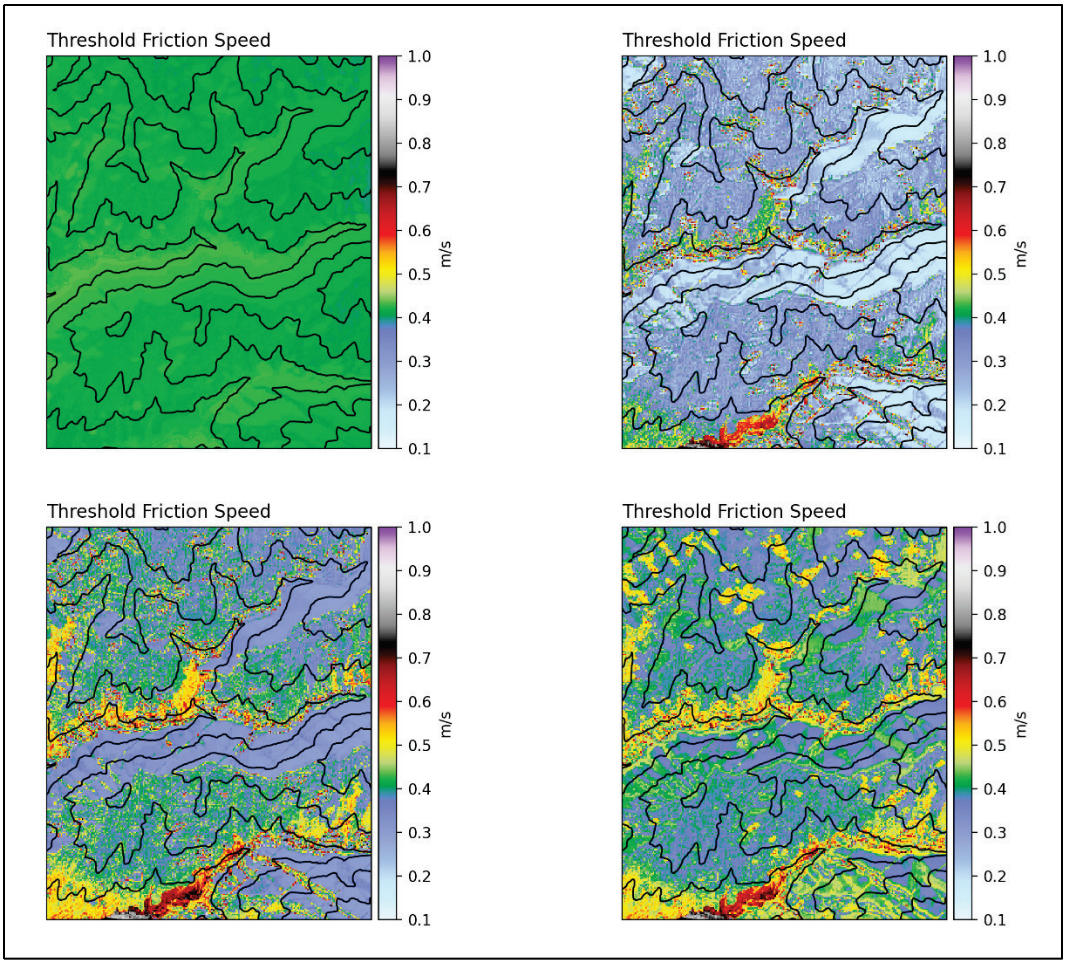

Figure 15. Simulated February mean snow depth for the control simulation (*top left*) and Δ snow depth for each of the experimental configurations. Elevation contours are shown in *black* with an 80 m interval.

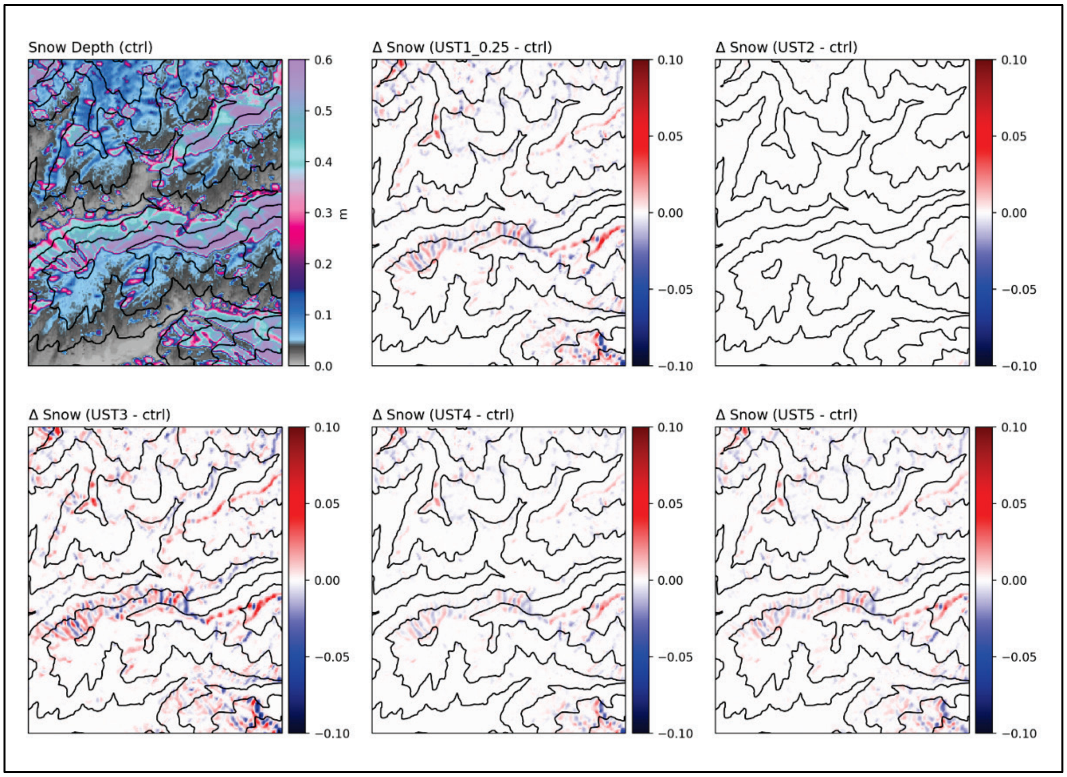

4 Discussion

The work here dramatically increases the capacity of Noah-MP as an environmental simulation tool in extreme cold environments. In particular, adding a snow transport overlay to the model makes it a more applicable tool for tactical-scale environmental modeling in regions with complex terrain. Further, because Noah-MP is a comprehensive land model, it is better suited than models specific to snow to simulate an integrated surface state. In particular, we posit that these upgrades will improve integrated hydrology simulations in local-scale, snow-dominated watersheds with high relief. However, due to its relatively low number of snow layers and fixed layering system, Noah-MP is still likely not the best tool for simulating snowpack stratigraphy, despite the addition of the snow microstructure parameterizations. We suspect that models with more advanced snow layering schemes, such as SNOWPACK, Crocus, or SnowModel, are likely better options when detailed snow stratigraphy is a desired output.

The most critical component for accurately simulating snow transport on the tactical scale is the representation of micrometeorological variation in the wind field. Without microscale wind variability, the transport scheme will have little-to-no effect. In this study, we used the relatively simple wind downscaling procedure used as part of MicroMet (Liston and Elder 2006b). This generates micrometeorological variations in the wind field through minor adjustments due to terrain slope and aspect. However, recently, more advanced downscaling procedures have been made available. For example, WindNinja (Forthofer et al. 2014; Wagenbrenner et al. 2016) uses a momentum- and mass-conserving dynamic downscaling approach to simulate channel flows and buoyancy driven winds in complex terrain. We speculate that the effects of snow transport within Noah-MP could be better assessed when coupled with the WindNinja downscaling tool.

5 Conclusions

In this report, we described modifications added to the Noah-MP LSM to represent more detailed snow processes. These modifications were made to enable Noah-MP to be used for more focused snow studies in the future. In particular, the addition of a blowing snow transport overlay likely increased the realism of Noah-MP snow simulations over watershed scale domains at very high resolution. Idealized test simulations showed that the model generates results consistent with accepted snow transport behavior that favors the accumulation of blowing snow downwind of topographic crests.

Simulations of snow over the DCEW showed that Noah-MP was able to successfully simulate the evolution of the snow depth within the domain; however, snow cover extent was generally overestimated in Noah-MP when compared to Landsat-derived snow cover area maps. Further validation with high-resolution distributed snow depth maps from, for example, lidar could help inform the selection of the threshold friction speed parameters for different domains.

These model upgrades were incorporated to work with the HRLDAS drivers for the Noah-MP LSM and performed reliably when compiled with parallel MPI capability using the Fortran Intel compilers on a Cray-XE super computing system.

We hope that these upgrades enable and facilitate ongoing and future research aimed at characterizing the effects of the integrated snow and soil land surface in extreme cold environments at the tactical scale.

References

Anderson, B. T., J. P. McNamara, H.-P Marshall, and A. N. Flores. 2014. “Insights into the Physical Processes Controlling Correlations between Snow Distribution and Terrain Properties.” *Water Resources Research* 50 (6): 4,545–4,563. https://doi.org/10.1002/2013WR013714.

Barlage, M., F. Chen, M. Tewari, K. Ikeda, D. Gochis, J. Dudhia, R. Rasmussen, B. Livneh, M. Ek, and K. Mitchell. 2010. “Noah Land Surface Model Modifications to Improve Snowpack Prediction in the Colorado Rocky Mountains.” *Journal of Geophysical Research: Atmospheres* 115 (D22). https://doi.org/10.1029/2009JD013470.

Boise State University. n.d. *Dry Creek Data* [Database]. https://www.boisestate.edu/drycreek/dry-creek-data/.

Brown, R. L., P. K. Satyawali, M. Lehning, and P Bartelt. 2001. “Modeling the Changes in Microstructure of Snow during Metamorphism.” *Cold Regions Science and Technology* 33 (2-3): 91–101. https://doi.org/10.1016/S0165-232X(01)00032-5.

Brun, E., P. David, M. Sudul, and G. Brunot. 1992. “A Numerical Model to Simulate Snow-Cover Stratigraphy for Operational Avalanche Forecasting.” *Journal of Glaciology* 38 (128): 13–22. https://doi.org/10.3189/S0022143000009552.

Cai, X., Z.-L. Yang, Y. Xia, M. Huang, H. Wei, L. R. Leung, and M. B. Ek. 2014. “Assessment of Simulated Water Balance from Noah, Noah-MP, CLM, and VIC over CONUS Using the NLDAS Test Bed.” *Journal of Geophysical Research: Atmospheres* 119 (24): 13,751–13,770. https://doi.org/10.1002/2014JD022113.

Clifton, A., J.-D. Rüedi, and M. Lehning. 2006. “Snow Saltation Threshold Measurements in a Drifting-Snow Wind Tunnel.” *Journal of Glaciology* 52 (179): 585–596. https://doi.org/10.3189/172756506781828430.

Comola, F., J. F. Kok, J. Gaume, E. Paterna, and M. Lehning. 2017. “Fragmentation of Wind-Blown Snow Crystals.” *Geophysical Research Letters* 44 (9): 4,195–4,203. https://doi.org/10.1002/2017GL073039.

Déry, S. J., and P. A. Taylor. 1996. “Some Aspects of the Interaction of Blowing Snow with the Atmospheric Boundary Layer.” *Hydrological Processes* 10 (10): 1,345–1,358. https://doi.org/10.1002/(SICI)1099-1085(199610)10:10%3C1345::AID-HYP465%3E3.0.CO;2-2.

Déry, S. J., and M. K. Yau. 1999. “A Bulk Blowing Snow Model.” *Boundary-Layer Meteorology* 93 (2): 237–251. https://doi.org/10.1023/A:1002065615856.

Dickinson, R. E., A. Henderson-Sellers, and P. J. Kennedy. 1993. *Biosphere-Atmosphere Transfer Scheme (BATS) Version 1e as Coupled to the NCAR Community Climate Model*. NCAR/TN-387+STR. Boulder, CO: National Center for Atmospheric Research. http://dx.doi.org/10.5065/D67W6959.

Essery, R., L. Li, and J. Pomeroy. 1999. "A Distributed Model of Blowing Snow over Complex Terrain." *Hydrological Processes* 13 (14-15), 2,423–2,438. https://doi.org/10.1002/(SICI)1099-1085(199910)13:14/15%3C2423::AID-HYP853%3E3.0.CO;2-U.

Forthofer, J. M., B. W. Butler, and N. S. Wagenbrenner. 2014. "A Comparison of Three Approaches for Simulating Fine-Scale Surface Winds in Support of Wildland Fire Management. Part I: Model Formulation and Comparison Against Measurements." *International Journal of Wildland Fire* 23 (7): 969–981. https://doi.org/10.1071/WF12089.

Golubev, V. N., and S. A. Sokratov. 2004. "Regular Packing of Grains as a Model of Snow Structure." *Annals of Glaciology* 38 (2004): 25–29. https://doi.org/10.3189/172756404781815004.

He, S., and N. Ohara. 2017. "A New Formula for Estimating the Threshold Wind Speed for Snow Movement." *Journal of Advances in Modeling Earth Systems* 9 (7): 2,514–2,525. https://doi.org/10.1002/2017MS000982.

Hedstrom, N. R., and J. W. Pomeroy. 1998. "Measurements and Modelling of Snow Interception in the Boreal Forest." *Hydrological Processes* 12 (10-11): 1,611–1,625. https://doi.org/10.1002/(SICI)1099-1085(199808/09)12:10/11%3C1611::AID-HYP684%3E3.0.CO;2-4.

Jordan, R. E. 1991. A One-Dimensional Temperature Model for a Snow Cover: Technical Documentation for SNTHERM.89. SR-91-16. Hanover, NH: US Army Engineer Research and Development Center, Cold Regions Research and Engineering Laboratory. http://hdl.handle.net/11681/11677.

Keenan, E., N. Wever, J. Lenaerts, and B. Medley. 2022. "A Wind-Driven Snow Redistribution Module for Alpine3D V3.3.0: Adaptations Designed for Downscaling Ice Sheet Surface Mass Balance." *Geoscientific Model Development* 16 (11): 3,303–3,219. https://doi.org/10.5194/gmd-16-3203-2023.

Kormos, P. R., D. Marks, J. P. McNamara, H. P. Marshall, A. Winstral, and A. N. Flores. 2014. "Snow Distribution, Melt and Surface Water Inputs to the Soil in the Mountain Rain–Snow Transition Zone." *Journal of Hydrology* 519 (2014): 190–204. https://doi.org/10.1016/j.jhydrol.2014.06.051.

Lehning, M., P. Bartelt, B. Brown, and C. Fierz. 2002. "A Physical SNOWPACK Model for the Swiss Avalanche Warning. Part III: Meteorological Forcing, Thin Layer Formation and Evaluation." *Cold Regions Science and Technology* 35 (3): 169–184. https://doi.org/10.1016/S0165-232X(02)00072-1.

Lehning, M., P. Bartelt, B. Brown, C. Fierz, and P. Satyawali. 2002. "A Physical SNOWPACK Model for the Swiss Avalanche Warning: Part II. Snow Microstructure." *Cold Regions Science and Technology* 35 (3): 147–167. https://doi.org/10.1016/S0165-232X(02)00073-3.

Lehning, M., and C. Fierz. 2008. "Assessment of Snow Transport in Avalanche Terrain." *Cold Regions Science and Technology* 51 (2-3): 240–252. http://dx.doi.org/10.1016/j.coldregions.2007.05.012.

Letcher, T. W., J. B. Eylander, and S. Shoop. 2022. "Are the Noah and Noah-MP Land Surface Model Soil Models Accurate under Frozen Conditions?" In *Proceedings 102nd American Meteorological Society Annual Meeting*, 23–27 January, Houston, Texas. Boston, MA: American Meteorological Society.

Letcher, T. W., J. R. Minder, and P. Naple. 2022. *Understanding and Improving Snow Processes in Noah-MP over the Northeast United States via the New York State Mesonet*. ERDC/CRREL TR-22-9. Hanover, NH: US Army Engineer Research and Development Center, Cold Regions Research and Engineering Laboratory. http://dx.doi.org/10.21079/11681/45060.

Li, L., and J. W. Pomeroy. 1997. "Estimates of Threshold Wind Speeds for Snow Transport using Meteorological Data." *Journal of Applied Meteorology and Climatology* 36 (3): 205–213. https://doi.org/10.1175/1520-0450(1997)036%3C0205:EOTWSF%3E2.0.CO;2.

Liston, G. E., and K. Elder. 2006a. "A Distributed Snow-Evolution Modeling System (SnowModel)." *Journal of Hydrometeorology* 7 (6): 1,259–1,276. https://doi.org/10.1175/JHM548.1.

Liston, G. E., and K. Elder. 2006b. "A Meteorological Distribution System for High-Resolution Terrestrial Modeling (MicroMet)." *Journal of Hydrometeorology* 7 (2): 217–234. https://doi.org/10.1175/JHM486.1.

Liston, G. E., R. B. Haehnel, M. Sturm, C. A. Hiemstra, S. Berezovskaya, and R. D. Tabler. 2007. "Simulating Complex Snow Distributions in Windy Environments Using SnowTran-3D." *Journal of Glaciology* 53 (181): 241–256. https://doi.org/10.3189/172756507782202865.

Liston, G. E., and M. Sturm. 1998. "A Snow-Transport Model for Complex Terrain." *Journal of Glaciology* 44 (148): 498–516. https://doi.org/10.3189/S0022143000002021.

Marsh, C. B., J. W. Pomeroy, R. J. Spiteri, and H. S. Wheater. 2020. "A Finite Volume Blowing Snow Model for Use with Variable Resolution Meshes." *Water Resources Research* 56 (2): e2019WR025307. https://doi.org/10.1029/2019WR025307.

Milley, M. A., and G. B. O'Keefe. 2016. *Mountain Warfare and Cold Weather Operations*. ATP 3-90.97. Washington, DC: Headquarters Department of the Army. https://irp.fas.org/doddir/army/atp3-90-97.pdf.

Minder, J. R., T. W. Letcher, and S. M. Skiles. 2016. "An Evaluation of High-Resolution Regional Climate Model Simulations of Snow Cover and Albedo Over the Rocky Mountains, with Implications for the Simulated Snow-Albedo Feedback." *Journal of Geophysical Research: Atmospheres* 121 (15): 9,069–9,088. https://doi.org/10.1002/2016JD024995.

Mitchell, K. E., D. Lohmann, P. R. Houser, E. F. Wood, J. C. Schaake, A. Robock, B. A. Cosgrove, et al. 2004. "The Multi-Institution North American Land Data Assimilation System (NLDAS): Utilizing Multiple GCIP Products and Partners in a Continental Distributed Hydrological Modeling System." *Journal of Geophysical Research: Atmospheres* 109 (D7). https://doi.org/10.1029/2003JD003823.

NCAR (National Center for Atmospheric Research). 2018. "HRLDAS Release." *GitHub*. https://github.com/NCAR/hrldas-release/blob/release/HRLDAS/run/.

Niu, G.-Y., Z.-L. Yang, K. E. Mitchell, F. Chen, M. B. Ek, M. Barlage, A. Kumar, et al. 2011. "The Community Noah Land Surface Model with Multiparameterization Options (Noah-MP): 1. Model Description and Evaluation with Local-Scale Measurements." *Journal of Geophysical Research: Atmospheres* 116 (D12). https://doi.org/10.1029/2010JD015139.

Pomeroy, J. W. 1988. "Wind Transport of Snow." PhD diss., University of Saskatchewan. https://harvest.usask.ca/handle/10388/etd-10142010-083840.

Pomeroy, J. W., and E. Brun. 2001. "Physical Properties of Snow." In *Snow Ecology: An Interdisciplinary Examination of Snow-Covered Ecosystems*, edited by H. G. Jones, J. W. Pomeroy, D. A. Walker, and R. W. Hoham, 45–126. Cambridge, UK: Cambridge University Press. https://www.geobotany.org/library/pubs/PomeroyJW2001_snowecol_ch2.pdf.

Pomeroy, J. W., and D. M. Gray. 1990. "Saltation of Snow." *Water Resources Research* 26 (7): 1,583–1,594. https://doi.org/10.1029/WR026i007p01583.

Pomeroy, J. W., D. M. Gray, and P. G. Landine. 1993. "The Prairie Blowing Snow Model: Characteristics, Validation, Operation." *Journal of Hydrology* 144 (1-4): 165–192. https://doi.org/10.1016/0022-1694(93)90171-5.

Pomeroy, J. W., and D. H. Male. 1992. "Steady-State Suspension of Snow." *Journal of Hydrology* 136 (1-4): 275–301. https://doi.org/10.1016/0022-1694(92)90015-N.

Roy, A., A. Royer, B. Montpetit, P. A. Bartlett, and A. Langlois. 2013. "Snow Specific Surface Area Simulation using the One-Layer Snow Model in the Canadian Land Surface Scheme (CLASS)." *The Cryosphere* 7 (3): 961–975. https://doi.org/10.5194/tc-7-961-2013.

Schmidt, R. A. 1980. "Threshold Wind-Speeds and Elastic Impact in Snow Transport." *Journal of Glaciology* 26 (94): 453–467. https://doi.org/10.3189/S0022143000010972.

Schmidt, R. A. 1982. "Vertical Profiles of Wind Speed, Snow Concentration, and Humidity in Blowing Snow." *Boundary-Layer Meteorology* 23 (2): 223–246. https://doi.org/10.1007/BF00123299.

Schmidt, R. A. 1991. "Sublimation of Snow Intercepted by an Artificial Conifer." *Agricultural and Forest Meteorology* 54 (1): 1–27. https://doi.org/10.1016/0168-1923(91)90038-R.

Selkowitz, D., T. H. Painter, K. Rittger, G. Schmidt, and R. Forster. 2017. "The USGS Landsat Snow Covered Area Products: Methods and Preliminary Validation." In *Automated Approaches for Snow and Ice Cover Monitoring using Optical Remote Sensing*, edited by D. Selkowitz, 76–119. Salt Lake City, UT: University of Utah.

Vionnet, V., E. Brun, S. Morin, A. Boone, S. Faroux, P. Le Moigne, E. Martin, and J-M. Willemet. 2012. "The Detailed Snowpack Scheme Crocus and its Implementation in SURFEX V7.2." *Geoscientific Model Development* 5 (3): 773–791. https://doi.org/10.5194/gmd-5-773-2012.

Vionnet, V., E. Martin, V. Masson, G. Guyomarc'h, F. Naaim-Bouvet, A. Prokop, Y. Durand, and C. Lac. 2014. "Simulation of Wind-Induced Snow Transport and Sublimation in Alpine Terrain Using a Fully Coupled Snowpack/Atmosphere Model." *The Cryosphere* 8 (2): 395–415. http://dx.doi.org/10.5194/tc-8-395-2014.

Wagenbrenner, N. S., J. M. Forthofer, B. K. Lamb, K. S. Shannon, and B. W. Butler. 2016. "Downscaling Surface Wind Predictions from Numerical Weather Prediction Models in Complex Terrain with WindNinja." *Atmospheric Chemistry and Physics* 16 (8): 5,229–5,241. https://doi.org/10.5194/acp-16-5229-2016.

Warscher, M., U. Strasser, G. Kraller, T. Marke, H. Franz, and H. Kunstmann. 2013. "Performance of Complex Snow Cover Descriptions in a Distributed Hydrological Model System: A Case Study for the High Alpine Terrain of the Berchtesgaden Alps." *Water Resources Research* 49 (5): 2,619–2,637. https://doi.org/10.1002/wrcr.20219.

Wrzesien, M. L., T. M. Pavelsky, S. B. Kapnick, M. T. Durand, and T. H. Painter. 2015. "Evaluation of Snow Cover Fraction for Regional Climate Simulations in the Sierra Nevada." *International Journal of Climatology* 35 (9): 2,472–2,484. https://doi.org/10.1002/joc.4136.

Xue, M. 2000. "High-Order Monotonic Numerical Diffusion and Smoothing." *Monthly Weather Review* 128 (8): 2,853–2,864. https://doi.org/10.1175/1520-0493(2000)128%3C2853:HOMNDA%3E2.0.CO;2.

Yang, Z.-L., G.-Y. Niu, K. E. Mitchell, F. Chen, M. B. Ek, M. Barlage, L. Longuevergne, et al. 2011. "The Community Noah Land Surface Model with Multiparameterization Options (Noah-MP): 2. Evaluation Over Global River Basins." *Journal of Geophysical Research: Atmospheres* 116 (D12): D12110. https://doi.org/10.1029/2010JD015140.

You, Y., C. Huang, Z. Yang, Y. Zhang, Y. Bai, and J. Gu. 2020. “Assessing Noah-MP Parameterization Sensitivity and Uncertainty Interval across Snow Climates.” *Journal of Geophysical Research: Atmospheres* 125 (4): e2019JD030417. https://doi.org/10.1029/2019JD030417.

Abbreviations

AGL	Above ground level
BATS	Biosphere-Atmosphere Transfer Scheme
DCEW	Dry Creek Experimental Watershed
557WW	557 Weather Wing
fSCA	Fractional Snow-Covered Area
HPCMP	High-Performance Computing Modernization Program
HRLDAS	High Resolution Land Data Assimilation System
LIS	Land Information System
LSM	Land surface model
LWC	Liquid water content
MPI	Message-passing interface
M2020	Marsh (2020)
NAD83	North American Datum of 1983
NCAR	National Center for Atmospheric Research
NLDAS	National Land Data Assimilation System
Noah-MP	Noah-Multiparameterization
1D	One dimensional
PG1990	Pomeroy and Gray (1990)
P1993	Pomeroy et al. (1993)
SSA	Snow specific area
SWE	Snow water equivalent

UST	Threshold friction velocity

REPORT DOCUMENTATION PAGE

1. REPORT DATE
September 2023

2. REPORT TYPE
Final Technical Report (TR)

3. DATES COVERED

START DATE
FY22

END DATE
FY23

4. TITLE AND SUBTITLE
Incorporating Advanced Snow Microphysics and Lateral Transport into the Noah-Multiparameterization (Noah-MP) Land Surface Model

5a. CONTRACT NUMBER

5b. GRANT NUMBER

5c. PROGRAM ELEMENT
0602144A

5d. PROJECT NUMBER
BN8

5e. TASK NUMBER

5f. WORK UNIT NUMBER

6. AUTHOR(S)
Theodore W. Letcher and Julie Parno

7. PERFORMING ORGANIZATION NAME(S) AND ADDRESS(ES)
US Army Engineer Research and Development Center (ERDC)
Cold Regions Research and Engineering Laboratory (CRREL)
72 Lyme Road
Hanover, NH 03755

8. PERFORMING ORGANIZATION REPORT NUMBER
ERDC/CRREL TR-23-10

9. SPONSORING/MONITORING AGENCY NAME(S) AND ADDRESS(ES)
Headquarters, US Army Corps of Engineers
Washington, DC 20314-1000

10. SPONSOR/MONITOR'S ACRONYM(S)
USACE

11. SPONSOR/MONITOR'S REPORT NUMBER(S)

12. DISTRIBUTION/AVAILABILITY STATEMENT
Distribution Statement A. Approved for public release: distribution is unlimited.

13. SUPPLEMENTARY NOTES

14. ABSTRACT

The dynamic state of the land surface presents challenges and opportunities for military and civil operations in extreme cold environments. In particular, the effects of snow and frozen ground on Soldier and vehicle mobility are hard to overstate. Current authoritative weather and land models are run at global scales (i.e., dx > 10 km) and are of limited use at the Soldier scale (dx < 100 m). Here, we describe several snow physics upgrades made to the Noah-Multiparameterization (Noah-MP) community land surface model (LSM). These upgrades include a blowing snow overlay to simulate the lateral redistribution of snow by the wind and the addition of new prognostic snow microstructure variables, namely grain size and bond radius. These additions represent major upgrades to the snow component of the Noah-MP LSM because they incorporate processes and methods used in more specialized snow modeling frameworks. These upgrades are demonstrated in idealized and real-world applications. The test simulations were promising and show that the newly added snow physics replicate observed behavior with reasonable accuracy. We hope these upgrades facilitate ongoing and future research on characterizing the effects of the integrated snow and soil land surface in extreme cold environments at the tactical scale.

15. SUBJECT TERMS
Blizzards; Cold regions; Meteorology; Snow; Trafficability; Weather

16. SECURITY CLASSIFICATION OF:

a. REPORT
Unclassified

b. ABSTRACT
Unclassified

C. THIS PAGE
Unclassified

17. LIMITATION OF ABSTRACT
SAR

18. NUMBER OF PAGES
62

19a. NAME OF RESPONSIBLE PERSON

19b. TELEPHONE NUMBER (include area code)

STANDARD FORM 298 (REV. 5/2020)
PREVIOUS EDITION IS OBSOLETE.
Prescribed by ANSI Std. Z39.18